International Journal of Heat and Mass Transfer 216 (2023) 124511

Contents lists available at ScienceDirect

International Journal of Heat and Mass Transfer

journal homepage: www.elsevier.com/locate/ijhmt

Anomalously strong effects of plume contraction and material redeposition in nanosecond pulsed laser vaporization

Alexey N. Volkov [a,*], Zhibin Lin [b]

[a] Department of Mechanical Engineering, University of Alabama, 7th Avenue, Tuscaloosa, AL, 35487, USA
[b] MKS Instruments, Inc., 14523 SW Millikan Way, Beaverton, OR, 97005, USA

ARTICLE INFO

Keywords:
Pulsed laser vaporization
Vapor plume
Plume stopping
Plume contraction
Material redeposition
Kinetic simulations

ABSTRACT

Long-term dynamics of vapor plumes induced by irradiation of a copper target in argon background gas by nanosecond laser pulses is studied numerically based on a one-dimensional hybrid computational model. The model includes a thermal model of the irradiated target and a kinetic model of the gaseous plume flow. The latter is implemented in the form of the direct simulation Monte Carlo method. The simulations, performed at moderate laser fluences in the range from 1.5 to 4 Jcm^{-2} and background gas pressures between 0.01 and 1 bar, show that the long-term plume dynamics can be divided into three major stages: initial inertial expansion, plume contraction, and subsequent diffusive expansion. The simulations unexpectedly predict extremely strong effects of plume contraction, when the plume size can exhibit a two-fold reduction, and delayed material redeposition back to the irradiated surface, when $\sim$ 90% of vaporized material returns to the irradiated surface. Both plume contraction and delayed redeposition originate from the strong backward flow induced by the internal (secondary) shock wave that propagates from the mixing layer towards the irradiated surface. The major part of vaporized material condenses at the surface with a long time delay with respect to the laser pulse after the plume stopping and before the onset of diffusive expansion. As a result, only a marginal part of vapor, which can be as small as $\sim$ 5%, is retained in the plume by the beginning of the diffusive expansion. The obtained simulation results suggest that the plume contraction and delayed material redeposition are common phenomena for nanosecond laser vaporization and may affect the efficiency and quality of laser surface modification in the ablation regime as well.

1. Introduction

The nanosecond pulsed laser ablation is the material removal process induced by heating of a material target by nanosecond pulses of laser radiation. The laser-induced ablation processes are broadly used in technological applications, from laser material processing [1] to pulsed laser deposition (PLD) of thin films [2], and in analytical applications for the analysis of the material composition, e.g., in the laser-induced breakdown spectroscopy (LIBS) [3]. The laser heating induces vaporization of the target material and expansion of a plume of ablation products into a vacuum or background gas. In material removal applications, the plume expansion process affects the degree of plasma shielding that occurs due to the absorption of incident laser radiation in the plume [4], radiative and conduction heating and etching of the target by plasma plume [5], expulsion of the molted material from the center of ablation crater under the recoil effect of vaporization and transient buildup of the plume pressure at the surface of the molten pool [6], as well as contamination of the processed targets with debris of the ablated material [7,8]. At a relatively small laser fluence, typically from 1 to a few Jcm^{-2}, the material removal occurs in the regime of surface vaporization, when the ablated plume consists of individual atoms.

After termination of the laser pulse and evaporation from the surface, the vapor plume expands inertially due to the strong pressure buildup in the initial vapor "bubble." For example, at a moderate pulse duration and laser fluence, the typical vapor number density at the end of the nanosecond laser pulse near the irradiated copper surface is on the order of $10^{20} - 10^{21}$ cm^{-3} [9,10], which corresponds to a pressure of 10–100 bar [9]. The interaction of the expanding plume with a background gas induces the formation of shock waves and a mixing layer at the boundary between the vapor and background gas, as well as gradual deceleration of the expansion process since the energy initially stored in the plume is continuously transferred to the background gas. The

* Corresponding author.
E-mail address: avolkov1@ua.edu (A.N. Volkov).

https://doi.org/10.1016/j.ijheatmasstransfer.2023.124511
Received 7 March 2023; Received in revised form 6 July 2023; Accepted 13 July 2023
Available online 3 August 2023

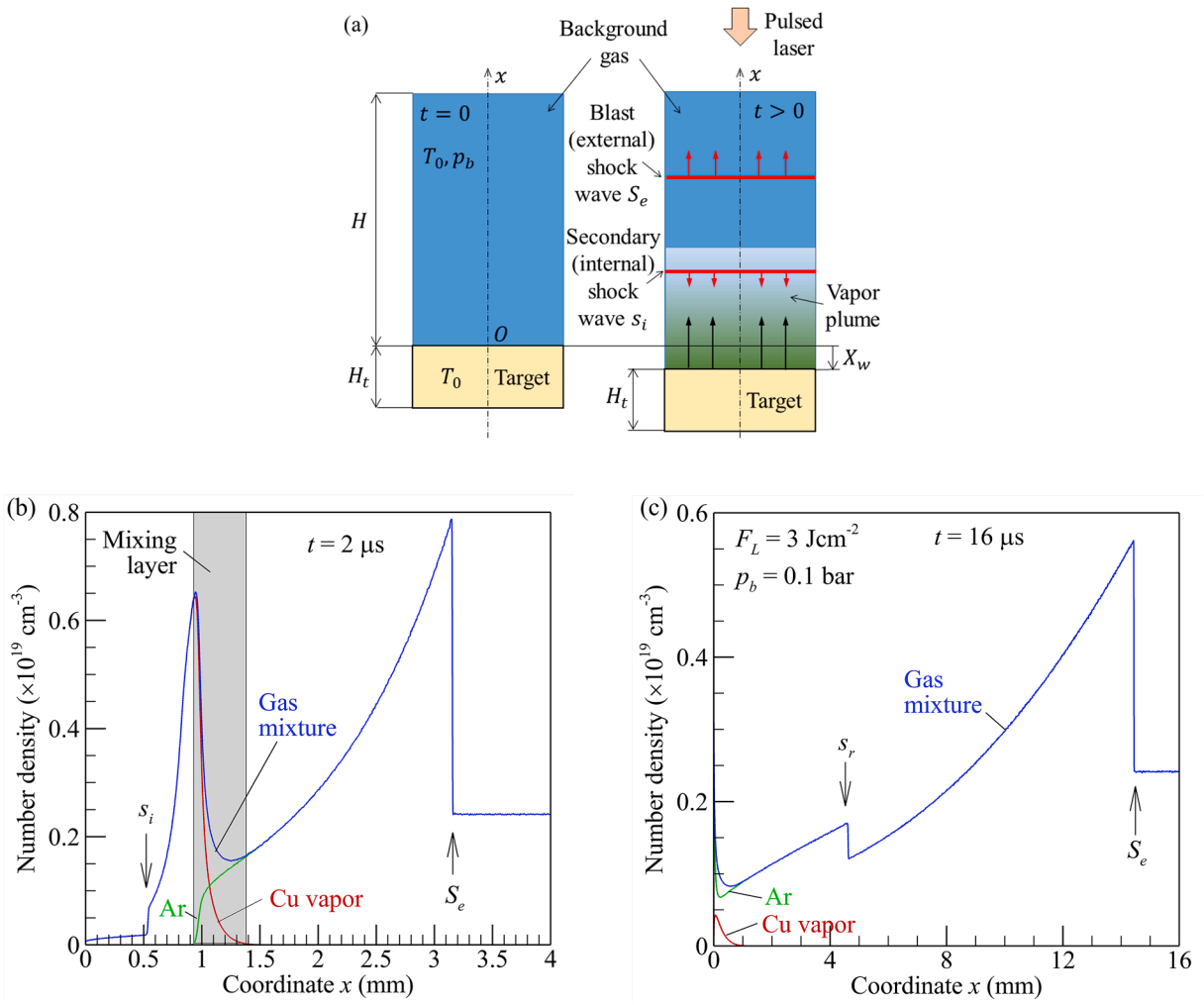

Fig. 1. (a) Sketch of the computational domain for 1D simulations of laser-induced plume expansion before the onset of irradiation ($t = 0$), when the whole system is kept at a temperature T_0 and the background gas pressure is equal to p_b, and during expansion of the plume ($t > 0$). The red horizontal lines with arrows schematically show the primary (external) shock wave S_e propagating from the irradiated target through the background gas and secondary (internal) shock wave s_i propagating towards the target through the plume. H and H_t are the sizes of the computational domains used for simulations of plume expansion and thermal state of the target, respectively. X_w is the ablation depth. The sizes of the gas-dynamic and target computational domains as well as ablation depth are shown not to scale; in actual simulations, $X_w \ll H_t \ll H$. Panels (b) and (c) show typical distributions of the Cu vapor n_{Cu} (red curves), Ar background gas n_{Ar} (green curves), and gas mixture $n = n_{Cu} + n_{Ar}$ (blue curves) number densities, when the secondary shock moves towards the surface and transformed into the reflected shock s_r, respectively. These distributions are obtained at a time of 2 μs (b) and 16 μs (c) for $F_L = 3$ Jcm^{-2} and $p_b = 0.1$ bar. In panel (b), the gray rectangle corresponds to the mixing layer, where the molar fraction of vapor varies from 1% to 99%.

stopping effect of the background gas results in the termination of the plume growth [11,12]. The maximum size of the plume in the direction normal to the irradiated surface and corresponding time are referred to as the plume stopping distance and time.

This initial stage of the plume expansion process from the onset of evaporation roughly until plume stopping is well-studied both experimentally, e.g., [13,14,15], and in simulations based on hydrodynamic, e.g., [14,16-22], and kinetic, e.g., [11,23-30], models of gas or plasma flows. The initial stage of the plume expansion process can be also approximately described by one-dimensional algebraic or semi-algebraic hydrodynamic models. Such models are based on the exact or approximate solution of the one-dimensional (1D) expansion problem into a vacuum [31,32] or background gas and approximate representations of the plume parameter distributions in regions separated by the shock waves and contact surfaces and subsequent solutions of the integral hydrodynamics equations. Currently, these models are available for both spherically symmetric [33] and planar [29] plumes.

The further evolution of the laser-induced plumes after stopping is marginally studied both experimentally and numerically. Such long-term plume dynamics, however, is relevant to multiple applications, e.g., to PLD of functional thin films [22,34,35], surface nanostructuring [36], and generation of nanoclusters due to vapor condensation in the plume [37]. The understanding of the long-term plume dynamics is also crucial for materials processing in the multi-pulse regime [38–40], where the plumes generated by preceding pulses change the environment for the expansion of plumes generated by subsequent pulses [9,41,42]. This effect was called the plume accumulation effect in Ref. [26]. In multi-pulse laser ablation, the pulse repetition rate varies in an extremely broad range, from sub-kHz to GHz and above [38–40], so that the inter-pulse separation time can be shorter or longer than the plume stopping time.

It is often accepted that, once the stopping effect ceases the inertial expansion of a plume, the plume size only slowly increases due to molecular diffusion of vapor into a background gas. Although the approximate hydrodynamics model predicts the contraction of a spherically symmetric plume [33], the degree of transient contraction of laser-induced plumes, as well as the consequences of this process for the redistribution of the ablated material inside the plume and its

condensation at the irradiated surface, practically remain unknown.

The goal of the present work is to investigate the long-term dynamics of vapor plumes induced by irradiation of a target by a nanosecond laser pulse in the regime of surface vaporization, to study the transition from initial inertial expansion to diffusive expansion, and to quantify the effect of material redeposition. For this purpose, the kinetic simulations of the plume expansion process based on the direct simulation Monte Carlo (DSMC) method [43] are performed. The DSMC method is a stochastic particle-based numerical approach developed in agreement with the Boltzmann equation [44]. In the DSMC method, gas is considered as a set of simulated particles that represent individual gas atoms or molecules, which move, participate in binary collisions, and interact with interphase boundaries. The DSMC method is usually used to simulate gas flows under conditions of strong rarefaction and non-equilibrium. In the laser-induced plume expansion problem, with decreasing background gas pressure, the continuum hypothesis breaks down in large regions inside the expanding plume, and the continuum gas dynamics description of the plume flow fails. More importantly, the zones with extremely low plume pressure can transiently appear inside the plumes even under conditions of atmospheric background gas pressure [9,25]. The kinetic models also naturally account for the formation of the Knudsen layer that emerges on surfaces subjected to fast evaporation or condensation [45]. This makes the kinetic models preferable over their hydrodynamics counterparts for high-fidelity simulations of laser-induced plume expansion. In the present work, the kinetic simulations of the plume expansion process at moderate background gas pressures are performed on a time scale from a few to a hundred of microseconds.

As it is the first study of such kind, we limit consideration to only 1D planar plume expansion, so that the obtained results are quantitatively valid in the limit of large laser spot sizes. The simulations show that the initial inertial expansion is separated from the diffusive expansion by a relatively long contraction stage, when the size of the vapor plume reduces by 30–50%. During the plume contraction, a strong back flow directed towards the surface of the irradiated target is developed. This flow augments redeposition of the ablated material back to the irradiated surface. As a result, the long-term dynamics of laser-induced plumes is always accompanied by unexpectedly strong condensation of vapor on the irradiated target, where up to 90% of the vaporized mass can return to the target surface.

2. Computational model

The computational model adopted in the present paper is based on the assumptions that the explosive fragmentation of the irradiated target and optical breakdown, e.g. [46], do not occur. For the irradiation parameters considered, these assumptions are verified in the preliminary simulations (Section 2.2). Then the simulations of the laser-induced plume expansion process are performed using a 1D hybrid computational model consisting of a thermal model of the irradiated target and a kinetic model of the plume flow [9]. In the thermal model, the unsteady heat conduction equation is solved to determine the temperature at the target surface and mass flux of evaporated material. This model is described in Appendix A. The kinetic model of two-component gas mixture flow is based on the Boltzmann kinetic equation generalized for a monatomic gas mixture and implemented in the form of the DSMC method. Both models are coupled with each other through the boundary conditions that express the mass and energy balance at the irradiated surface.

2.1. Kinetic model of plume expansion

The expansion of laser-induced vapor plume into a background gas is simulated in the 1D computational domain of size H placed on the top of the irradiated target (Fig. 1(a)). At the initial time $t = 0$, the whole domain above the target is filled with a background gas at a pressure p_b and temperature T_0.

Both the background gas and vapor are considered as monatomic gases. In the present work, the DSMC algorithm of sampling of velocities of gas particles after a binary collision is based on the preliminary calculated tables of the deflection angle as suggested in Ref. [47]. The deflection angle as a function of the relative particle speed C_r and geometric collision parameter b for Cu-Cu and Ar-Ar collisions was determined in Ref. [48] based on corresponding potential energy curves (PECs). These PECs were established in *ab initio* density functional theory (DFT) calculations with van der Waals corrections. For Cu-Ar collisions, the deflection angle was calculated based on the *ab initio* PEC obtained in Ref. [49] using quantum Monte-Carlo (QMC) calculations. The DFT and QMC PECs for Cu-Cu and Ar-Ar atom pars are found to be only marginally different [49]. In simulations, for each pair of colliding particles, their relative speed C_r and random collision parameter b were used as input to determine the deflection angle from a look-up table. Then the post-collisional velocities of particles were calculated using the equations, which can be found, e.g., in Ref. [43]. Further details of this approach are provided in Appendix B and can be also found in Refs. [47, 48]. The No Time Counter (NTC) scheme is used for sampling of binary collisions between simulated particles [43]. The calculations are performed with a parallel DSMC code, which was previously developed for simulations of the 1D laser-induced plume expansion process and used, e.g., in Refs. [9,28,47].

The kinetic boundary conditions at the irradiated surface account for evaporation, condensation, and reflection of gas atoms. The Hertz-Knudsen model [45] with an evaporation coefficient equal to 1 is used to describe evaporation and to generate new simulated vapor atoms at the target surface during each time step of computations. According to this model, the velocity distribution function of vapor atoms, $f_{v(e)}(x,\mathbf{v},t)$, emitted from the evaporating surface, is a half-Maxwellian distribution at the surface temperature T_w:

$$\text{At } x=0,\ v_x>0:\ f_{v(e)}(0,\mathbf{v},t)=\frac{p_v(T_w)/(k_BT_w)}{(2\pi(k_B/m_v)T_w)^{3/2}}\exp\left(-\frac{m_v\mathbf{v}^2}{2k_BT_w}\right), \tag{1}$$

where t is the time, x is the coordinate counted along the flow direction (Fig. 1(a)), $\mathbf{v}=(v_x,v_y,v_z)$ is the molecule velocity vector, m_v is the mass of a vapor atom, $p_v(T_w)$ is the saturated vapor pressure determined by the Clausius-Clapeyron equation [Eq. (A.5)], and k_B is the Boltzmann constant. Then the evaporation number density flux J_e is defined by Eq. (A.4).

The condensation coefficient α_c is equal to the fraction of incident vapor atoms that is absorbed by the surface. Then the condensation flux J_c in Eq. (A.3), number flux density of atoms condensing at the surface, is equal to

$$J_c=\alpha_c\int\limits_{v_x<0}|v_x|f_v(0,\mathbf{v},t)d\mathbf{v}. \tag{2}$$

The fraction $1-\alpha_c$ of vapor atoms incident to the irradiated surface is assumed to be diffusely scattered and returned back to the flow, so that the velocity distribution function of reflected vapor atoms is equal to [50]:

$$\text{At } x=0,\ v_x>0:\ f_{v(r)}(0,\mathbf{v},t)=(1-\alpha_c)\frac{2}{\pi}\exp\left(-\frac{\mathbf{v}^2}{C_v^2}\right)\int\limits_{v_x'<0}\frac{|v_x'|}{C_v^4}f_v(0,\mathbf{v}',t)d\mathbf{v}', \tag{3}$$

where $C_v=\sqrt{2k_BT_w/m_v}$. The boundary conditions for vapor atoms at the irradiated surface then read

$$\text{At } x=0,\ v_x>0:\ f_v(0,\mathbf{v},t)=f_{v(e)}(0,\mathbf{v},t)+f_{v(r)}(0,\mathbf{v},t). \tag{4}$$

The condensation coefficient α_c can strongly affect the long-term dynamics of vapor plumes. The value of α_c, however, remains a poorly defined quantity. At equilibrium, the net mass flux at the liquid-vapor or

solid-vapor interface is zero, and the evaporation and condensation coefficients are equal to each other. The common approach is, therefore, to set both evaporation and condensation coefficients equal to 1. The available experimental data confirm that the sticking coefficients of metals at room temperature are close to 1 [51,52], however, α_c can significantly reduce at elevated temperatures [53]. The temperature dependence of α_c for copper, used as the target material in the present work, is currently unknown, therefore, the parameter α_c is considered as a model parameter. The effect of α_c on the long-term plume dynamics is considered in Section 3.6.

The interaction of the background gas atoms with the irradiated surface is described by the model of diffuse scattering:

$$\text{At } x=0,\ v_x>0:\ f_b(0,\mathbf{v},t)=\frac{2}{\pi}\exp\left(-\frac{\mathbf{v}^2}{C_b^2}\right)\int\limits_{v_x'<0}\frac{|v_x'|}{C_b^4}f_b(0,\mathbf{v}',t)d\mathbf{v}', \tag{5}$$

where $f_b(\boldsymbol{x},\mathbf{v},t)$ is the velocity distribution function of the background gas atoms, $C_b=\sqrt{2k_BT_w/m_b}$, and m_b is the mass of a background gas atom.

The boundary conditions at the top boundary of the computational domain placed at a distance H from the target describe the gas exchange between the computational domain and a reservoir, where the background gas rests in equilibrium at a pressure p_b and temperature T_0 with zero macroscopic velocity. Then, at the exit boundary of the computational domain, $x=H$, the velocity distribution function of the background gas atoms, entering the domain through this boundary, is assumed to be a half-Maxwellian at a temperature T_0 and pressure p_b:

$$\text{At } x=H,\ v_x<0:\ f_b(H,\mathbf{v},t)=\frac{p_b/(k_BT_0)}{(2\pi(k_B/m_b)T_0)^{3/2}}\exp\left(-\frac{m_b\mathbf{v}^2}{2k_BT_0}\right). \tag{6}$$

All gas particles, leaving the domain through the exit boundary, are excluded from further computations. In simulations, the size of the computational domain H is chosen to be sufficiently large to ensure that the primary shock wave, propagating through the background gas, does not reach the external boundary during the simulated process time.

2.2. Simulation parameters

The simulations are performed for a copper target in argon background gas irradiated by a Gaussian laser pulse at a wavelength of 266 nm and intensity

$$I_L(t)=\frac{F_L}{\sqrt{2\pi}\sigma_t}\exp\left[-\frac{(t-t_{max})^2}{2\sigma_t^2}\right], \tag{7}$$

where $\sigma_t=\tau_L/(2\sqrt{2\log 2})$, τ_L is the pulse duration (FWHM), F_L is the laser fluence, and $t_{max}=3\sigma_t$ is the time when the laser intensity is maximum. The thermal and optical properties of the irradiated material, which are used in the present work, can be found in Refs. [9,26].

The simulations are performed at $\tau_L=10$ ns ($t_{max}=12.7$ ns), $T_0=300$ K, laser fluence F_L varying from 1.5 Jcm^{-2} to 4 Jcm^{-2}, and the background gas pressure p_b varying from 0.01 bar to 1 bar. The previous simulations [48] showed that, under these irradiation conditions, the maximum surface temperature varies from 3020 K to 7200 K (see also Appendix A) and remains smaller than $0.9T_c=7452$ K, where $T_c=8280$ K is the thermodynamic critical temperature of copper [54], so that the range of laser fluence under consideration is below the threshold for explosive boiling [55] and the assumption of material removal in the regime of surface evaporation holds. The preliminary simulations performed based on the computational approach, where the equilibrium ionization and radiation absorption models are combined with the DSMC method [10], also showed the irradiation conditions in the present paper are below the plasma shielding threshold. Most of the simulations are performed with the condensation coefficient $\alpha_c=1$. The results of simulations performed with $\alpha_c=0.5$ and 0 are described in Section 3.6.

To minimize the required computational resources, the length of the computational domain H and simulated process time t_E were chosen in preliminary simulations depending on the irradiation and environmental conditions. They were varied from $H=1$ mm and $t_E=2$ μs at the smallest F_L and largest p_b to $H=24$ mm and $t_E=100$ μs at the largest F_L and smallest p_b. These values guarantee that the external shock wave does not leave the domain during t_E, while t_E is long enough to observed the delayed deposition of the vaporized material. All DSMC simulations are performed with the same cell size of 50 nm and time step of 0.5 ps. The maximum total number of simulated particles N was varied in a range from $\sim 10^6$ to $\sim 10^8$, depending on the irradiation conditions and background gas pressure. For example, at $p_b=0.01$ bar, N was determined by the condition that 80 simulated particles of argon gas are present in average in each cell of the computational mesh before the onset of laser irradiation. The values of the DSMC cell size, time step, and the number of simulated particles that ensure numerical convergence of the simulation results were found in massive preliminary simulations. To reduce the statistical noise in unsteady simulations, for each set of input parameters, the simulations with different random seeds were repeated N_T times, where N_T varies in the range from 10 to 1000. Then the ensemble averaging of the results over N_T "trajectories" of the random process was performed to find the distributions of macroscopic plume parameters.

3. Results and discussion

3.1. Three stages of plume expansion: initial expansion, contraction, and further diffusive expansion

The flow structure during expansion of the plume obtained at $t=2$ μs for $F_L=3$ Jcm^{-2} and $p_b=0.1$ bar is illustrated in Fig. 1(b). It includes the primary (blast or external) shock wave S_e propagating through the background gas, secondary (internal) shock wave s_i propagating in the vapor plume towards the irradiated target, and a mixing layer, where the background gas mixes with vapor due to molecular diffusion. The mixing layer is always located between S_e and s_i. The secondary shock wave propagates with velocity U_i ($U_i<0$) towards the irradiated surface in the frame of reference which moves with local plume velocity u (u is the plume velocity right before the secondary shock wave). The velocity of this shock wave with respect to the target, $u+U_i$, can be either positive or negative depending on the pressure drop at this shock wave. The sign of $u+U_i$ and, correspondingly, the direction of motion of s_i with respect to the target change during the expansion process. Typically, once the secondary shock wave forms, it is relatively weak and $u+U_i>0$. Later, when the pressure in front of the s_i drops, the magnitude of U_i increases and this shock starts to approach the irradiated target. Under conditions considered in Fig. 1(b), the secondary shock wave appears near the mixing layer at a time ~ 0.2 μs as a result of deceleration of the plume caused by background gas. With respect to the irradiated surface, the secondary shock wave moves forward until ~ 1.5 μs. At a time of 2 μs, $u+U_i<0$ and s_i moves towards the target. Depending on the irradiation and environmental conditions, this shock may or may not reach the surface and be reflected from it. Earlier simulations under similar irradiations conditions but smaller F_L indicated no reflection of s_i from the surface, as this shock wave disappeared in the transient rarefaction zone near the surface [9]. Under condition illustrated in Fig. 1 (b), the secondary shock wave reaches the surface at $\tau_i\sim 3.3$ μs, inducing formation of a reflected shock s_r moving from the surface.

As known, the fall of an incident normal shock on a surface induces the formation of a reflected shock due to the surface impenetrability to the gas flow. In the present problem, the process of reflection is more complex when it is accompanied by the full or partial condensation of vapor on the surface. If the condensation coefficient is equal to zero ($\alpha_c=0$), the reflection occurs like in the classical case of impenetrable

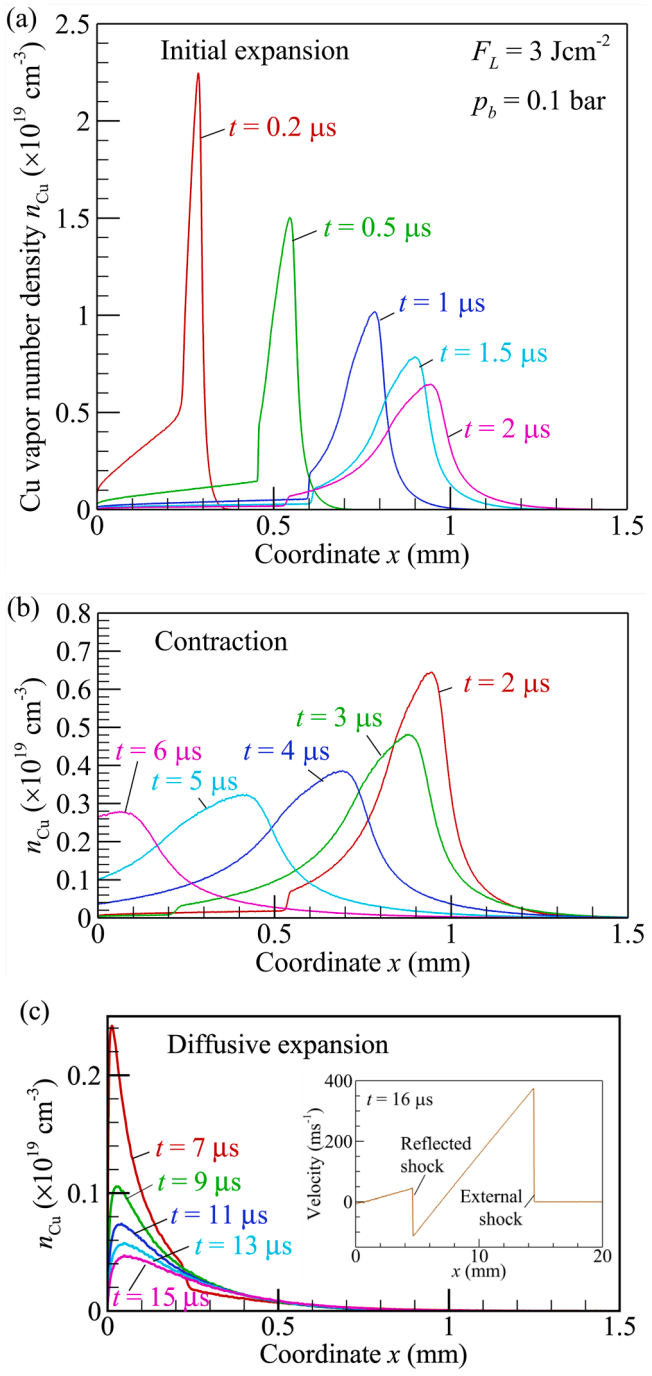

Fig. 2. Distributions of the number density n_{Cu} of Cu vapor at various times obtained for a laser fluence of $F_L = 3$ Jcm^{-2} and background gas pressure of $p_b = 0.1$ bar. The time for each curve is indicated in the figure panels. Individual panels contain curves corresponding to the initial expansion (a), contraction (b), and diffusive expansion (c) stages of the plume expansion process. In panel (c), the inset shows the distribution of gas mixture velocity at $t = 16$ μs.

surface immediately after the fall of the incident shock. In the case of the full condensation of vapor at the surface ($\alpha_c = 1$) shown in Figs. 1 and 2, the fall of the internal shock wave on the surface does not induce the immediate formation of the reflected shock. The reflected shock appears later, when the back flow of the non-condensable background gas induced by the internal shock reaches the surface. The reflected shock propagates first through the mixing layer and then moves in the background gas (Fig. 1(c)). The propagation of the external, internal, and reflected shock waves, including the delayed formation of the reflected shock, is further analyzed in Appendix C.

The consideration of the plume expansion process during long expansion time allows one to identify three characteristic stages of plume expansion, namely, initial expansion, contraction, and diffusive expansion of the plume. The variation of distributions of the copper vapor number density obtained at $F_L = 3$ Jcm^{-2} and $p_b = 0.1$ bar during these three stages is illustrated in individual panels of Fig. 2. The blast shock wave propagates through the background gas and cannot be seen in the distribution of vapor number density shown in Fig. 2.

During the initial expansion (Fig. 2(a)), the maximum of the copper vapor density, which is formed behind s_i near the internal boundary of the mixing layer, moves from the irradiation target, and the overall plume size increases. This stage of the plume expansion process can be also referred to as the inertial expansion, as it proceeds due to energy and pressure initially accumulated in the plume during the laser pulse. It occurs until ~ 2 μs, when the propagation speed of the density maximum drops almost to zero. The deceleration of expansion is caused by the stopping effect of the background gas and propagation of the secondary shock wave. As this shock wave starts to move towards the surface, a region with a relatively large flow velocity directed towards the surface develops in the plume behind this shock. Initially, the plume velocity is negative only right behind the shock, but the size of the zone with the negative velocity gradually expands and reaches the plume edge. At this time, the further expansion of the plume is terminated.

The stage of contraction (Fig. 2(b)) is characterized by negative bulk velocity everywhere inside the plume. The maximum of the vapor density moves towards the irradiated surface and reaches it at a time of ~ 6.5 μs. This process can strongly reduce the overall plume size. Under conditions considered in Fig. 2, the apparent size of the plume at ~ 6 μs exhibits roughly two-fold reduction from its maximum at the end of the initial expansion. The plume contraction is accompanied by strong redeposition of vapor back to the irradiated surface. Qualitatively, the contraction is terminated when the flow velocity everywhere in the plume becomes sufficiently small. The propagation of the reflected shock after the termination of contraction does not induce large velocity of the vapor component in the plume flow.

Once the contraction is terminated, the plume starts to slowly grow again due to molecular diffusion and mixing of vapor with the background gas under conditions of almost zero bulk flow velocity. At this stage of diffusive expansion (Fig. 2(c)), the maximum of vapor density is located near the irradiated surface. It appeared that there is a trade-off between diffusion of vapor from the surface and towards the surface, where the vapor continues to redeposit. The reflected shock wave can be seen in the distribution of vapor density at $t = 7$ μs. At later times, the reflected shock propagates outside the plume through the background gas. This shock can be seen in the distribution, e.g., of the gas mixture velocity shown in the inset of Fig. 2(c) for $t = 16$ μs. The negative velocity, which corresponds to the flow directed towards the irradiated surface, in the background gas in front of the reflected shock is developed during the previous contraction stage. Under conditions considered in the present work, a speed of the backward flow of the background gas of ~ 100 ms^{-1} has the order of magnitude of typical plume speed behind the internal shock wave.

3.2. Measures of the plume size

The analysis presented in Section 3.1 is to large extent qualitative, since it is not based on quantitative criteria that determine the transition from initial expansion to contraction and from contraction to diffusive expansion. To formulates such criteria, it is necessary to define a nominal plume size since the molecular diffusion is intrinsically accounted for in the kinetic simulations and there is no distinct contact surface separating the vapor and the background gas. Instead of the contact surface, the plume is terminated in a thick mixing layer, where the vapor density gradually drops to zero. The thickness of the mixing layer primarily depends on the characteristic mean free path of molecules in the

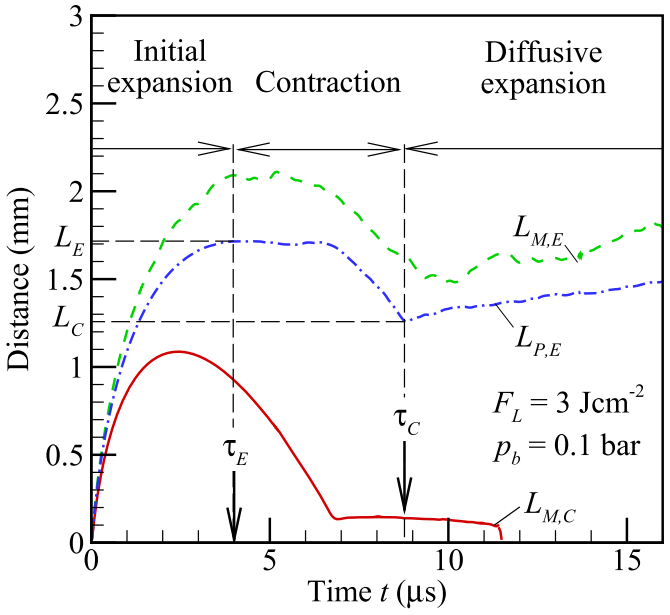

Fig. 3. Mixing layer center, $L_{M,C}$, (red solid curve) and edge, $L_{M,E}$, (green dashed curve) positions defined by Eq. (8) at $\varphi = 1/2$ and 0.0003, respectively, as well as integral plume size $L_{P,E}$ (blue dashed-dotted curve) calculated based on Eq. (11) at $\Phi = 0.9999$ versus time t. All results are obtained for $F_L = 3$ Jcm^{-2} and $p_b = 0.1$ bar. The whole plume expansion process is divided into the initial expansion, contraction, and diffusive expansion stages based on the results presented by the blue dashed-dotted curve. The vertical arrows mark the initial expansion (or plume stopping) time τ_E and contraction time τ_C that are defined as times when $L_{P,E}$ has the first local maximum and minimum, respectively. The corresponding plume sizes at the end of initial expansion and contraction are defined as $L_E = L_{P,E}(\tau_E)$ and $L_C = L_{P,E}(\tau_C)$, respectively.

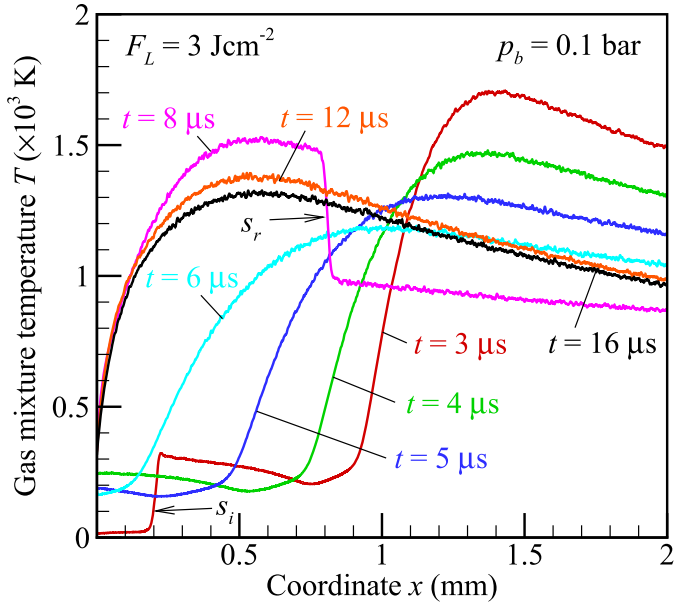

Fig. 4. Distributions of the gas mixture temperature T at various times obtained for a laser fluence of $F_L = 3$ Jcm^{-2} and background gas pressure of $p_b = 0.1$ bar. The time for each curve is indicated in the figure panel. s_i and s_r mark the positions of the internal (secondary) and reflected shock waves, respectively.

gas mixture and, thus, is determined by the gas mixture density at the edge of the plume.

The nominal plume size can be characterized by the maximum position of a surface $L_{M(\varphi)}$, where the molar fraction of vapor $\varphi_{\mathrm{Cu}}(x,t) = n_{\mathrm{Cu}}(x,t)/[n_{\mathrm{Cu}}(x,t) + n_{\mathrm{Ar}}(x,t)]$ is equal to some characteristic level φ, i.e., the following equation is satisfied:

$$\varphi_{\mathrm{Cu}}(L_{M(\varphi)}(t),t) = \varphi. \tag{8}$$

The choice of $\varphi = 1/2$ corresponds to the center of the mixing layer. The corresponding measure of the plume size $L_{M,C} = L_{M(1/2)}$ is shown in Fig. 3 by the red solid curve. The use of this measure can lead to incorrect conclusions about the variation of the plume size, especially at longer times, when, due to mutual diffusion of species, the molar fraction of vapor can be smaller than 1/2 everywhere. A reasonable measure of the plume size can be obtained by choosing such small threshold level φ that $L_{M(\varphi)}$ characterizes the position of an external boundary of the mixing layer, e.g., $\varphi = 3 \cdot 10^{-4}$. The corresponding measure of the plume size $L_{M,E} = L_{M(0.0003)}$ is shown in Fig. 3 by the green dashed curve. However, when φ is small, the calculated values of $L_{M,E}$ suffer from spurious oscillations due to the intrinsic statistical noise of the DSMC method.

To reduce the noise, an alternative definition of the plume size can be introduced based on the integral number of particles in the vapor plume between the irradiated surface and flow cross section with coordinate x:

$$\aleph_{\mathrm{Cu}}(x,t) = \int_0^x n_{\mathrm{Cu}}(x',t)dx', \tag{9}$$

so that the total number of vapor atoms at a time t in the plume is equal to

$$N_{\mathrm{Cu}}(t) = \aleph_{\mathrm{Cu}}(\infty,t). \tag{10}$$

Then the nominal plume size can be defined as the size of the domain $L_{P(\Phi)}$, which contains Φ fraction of all plume particles, i.e., as the position x of boundary where the fraction $\Phi_{\mathrm{Cu}}(x,t) = \aleph_{\mathrm{Cu}}(x,t)/N_{\mathrm{Cu}}(t)$ is equal to Φ:

$$\Phi_{\mathrm{Cu}}(L_{P(\Phi)}(t),t) = \Phi. \tag{11}$$

The integral plume size $L_{P,E} = L_{P(0.9999)}$ corresponding to $\Phi = 0.9999$ is shown in Fig. 3 by the blue dashed-dotted curve. By varying the threshold values of φ and Φ, the values of $L_{M,E}$ and $L_{P,E}$ can be brought into quantitative agreement with each other at fixed F_L and p_b. The values of φ and Φ required for agreement between $L_{M,E}$ and $L_{P,E}$, however, depend on F_L and p_b and, thus, there are no unique threshold values of φ and Φ that can provide agreement between $L_{M,E}$ and $L_{P,E}$ under various irradiation and environmental conditions.

For a given nominal plume size, the ends of the initial expansion and contraction stages can be associated with the local maximum and minimum of the plume size as a function of time, respectively. Under conditions illustrated in Fig. 2, the variations of both $L_{M,E}$ and $L_{P,E}$ indicate that the initial plume expansion is terminated at ~ 4 μs, while the plume contraction is terminated at a time between 8 μs and 9 μs. On the contrary, the varaition of $L_{M,C}$ shows the end of initial expansion at ~ 2 μs in agreement with the previous visual analysis of distributions in Fig. 2. The difference in the duration of the initial expansion stage predicted based on different definitions of the plume size is expected. During initial expansion, the point $x = L_{M,C}$, where $n_{\mathrm{Cu}}(L_{M,C},t) = n_{\mathrm{Ar}}(L_{M,C},t)$, is located somewhat ahead but near the vapor density maximum as seen, e.g., in Fig. 1(b). Therefore, the value of $L_{M,C}$ can be used to characterize the position of the major part of the plume associated with the vapor density maximum. The values of $L_{M,E}$ and $L_{P,E}$ characterize the position of the plume edge, where the vapor molar fraction is small. The increase in the position of the plume edge compared to the mxing layer center is strongly augmented by molecular diffusion of vapor into the background gas and increase in the thickness of the mixing layer with time.

The reduction of $L_{M,E}$ and $L_{P,E}$ during contraction indicates that the molecular diffusion cannot overcome the effect of the overall plume contraction, and the position of the very edge of the plume moves to-

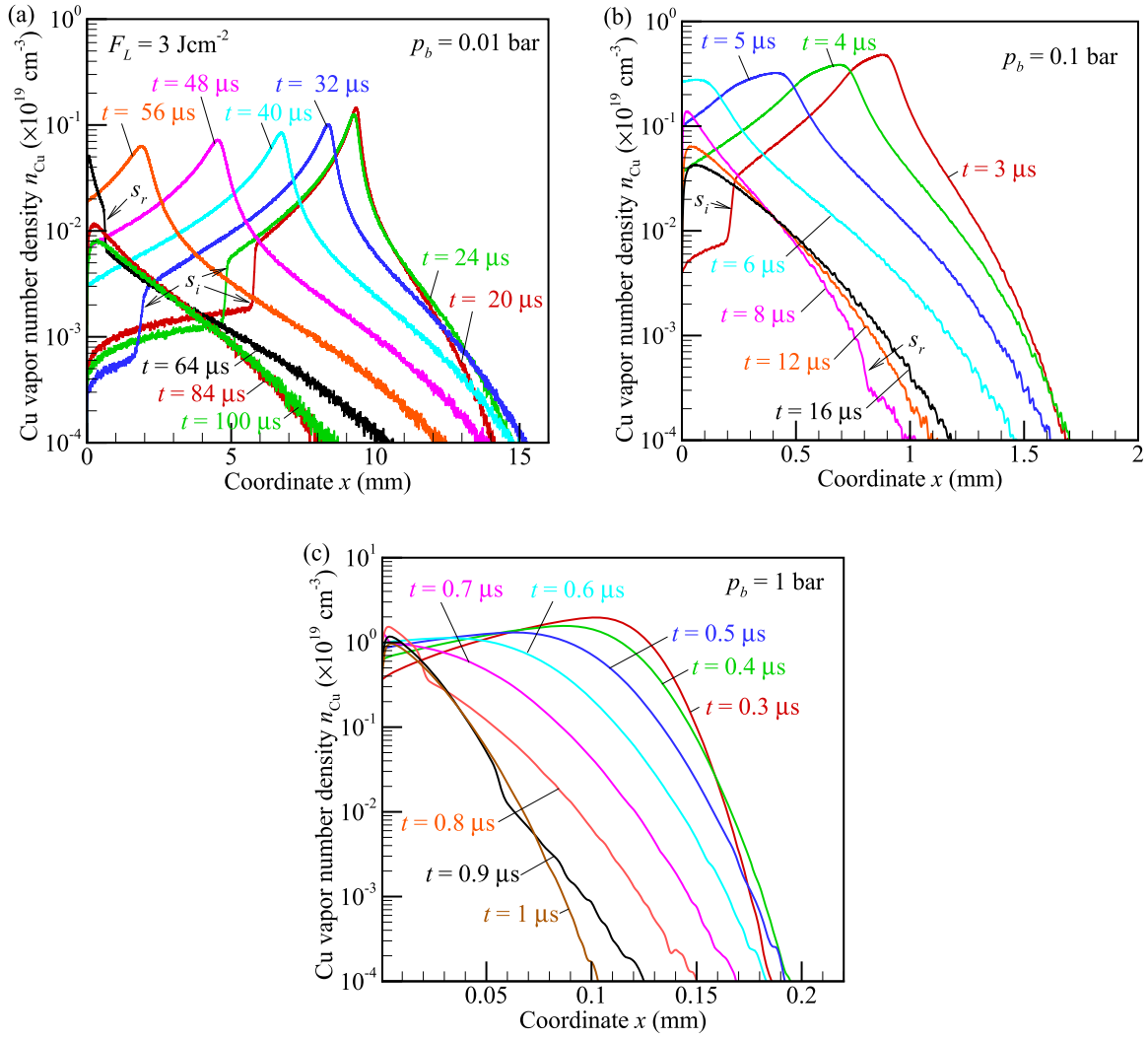

Fig. 5. Distributions of the number density n_{Cu} of Cu vapor at various times obtained for a laser fluence of $F_L = 3$ Jcm^{-2} and background gas pressure of $p_b = 0.01$ bar (a), 0.1 bar (b), and 1 bar (c). The time for each curve is indicated in the figure panels. In panels (a) and (b), s_i and s_r mark the positions of the internal (secondary) and reflected shock waves, respectively. In panel (b), some curves are taken from Fig. 2 and reproduced here to illustrate the variation of the vapor density at the plume edge.

wards the surface. One can also conclude that the whole contraction stage can be divided, in turn, into two parts: During the time from ~ 4 μs until ~ 6 μs, the position of the plume edge remains practically constant, while it reduced only during the following time, from ~ 6 μs until ~ 9 μs.

The value of $L_{P,E}(t)$ appeared to be the most reliable measure of the plume size. Hereinafter, the initial expansion time or plume stopping time τ_E and contraction time τ_C are therefore defined as times when $L_{P,E}$ has the first local maximum and minimum, respectively. The corresponding plume sizes at the end of initial expansion and contraction are defined as $L_E = L_{P,E}(\tau_E)$ and $L_C = L_{P,E}(\tau_C)$, respectively (Fig. 3). The value of L_E represents the plume stopping distance, while L_C is the minimum plume size at contraction.

The distributions of the gas mixture temperature shown in Fig. 4 indicate a relatively large temperature rise behind the reflected shock wave, e.g., at a time of 8 μs. The thermal homogenization of the plume, therefore, does not occur after disappearance of the internal shock wave and during the diffusive expansion stage. For instance, at $t = 16$ μs, the gas mixture temperature in the region occupied by the plume varies from ~ 300 K at the surface up to a maximum of ~ 1300 K inside the plume. At this time, however, inside the plume, the gas pressure is practically homogeneous, and the gas velocity is nearly zero.

To confirm the conclusion that the plume edge actually moves towards the target during the contraction stage in spite of molecular diffusion, a few distributions from Fig. 2(b) and (c) are replotted in the logarithmic scale in Fig. 5(b). These results show that, during the contraction stage, not only the nominal plume size reduces, but also the number density drops everywhere at $x > L_{P,E}(t)$, so that the contraction indeed overcomes the effect of diffusion.

3.3. Effect of the background gas pressure

The distributions of vapor density obtained at a background gas pressure of 0.01 bar, 0.1 bar, and 1 bar are compared in Fig. 5 for $F_L = 3$ Jcm^{-2}. The variation of background gas pressure induces the apparent variation in the plume size and duration of each stage of the expansion process.

These results also point to the qualitative difference between the vapor density distributions at $p_b = 0.1$ bar and 1 bar. The vapor density distributions at atmospheric pressure, in particular, do not show distinct traces of the internal and reflected shock waves. Despite this difference, the variation of the integral plume size $L_{P,E}$ with time indicates the existence of the contraction stage of finite duration independently of the background gas pressure (Fig. 6(a)). The reduction in the background gas pressure strongly increases the plume stopping distance L_E and

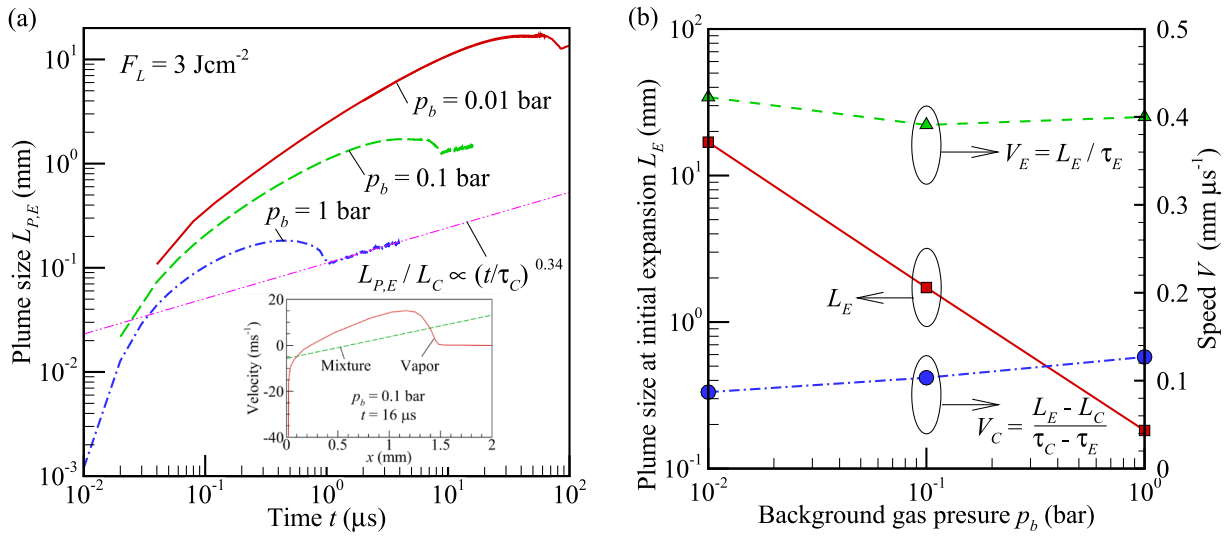

Fig. 6. (a), Integral plume size $L_{P,E}$ calculated based on Eq. (11) at $\Phi = 0.9999$ versus time t for a laser fluence of $F_L = 3$ Jcm^{-2} and background gas pressure of $p_b = 0.01$ bar (red solid curve), $p_b = 0.1$ bar (green dashed curve), and $p_b = 1$ bar (blue dashed-dotted curve). The magenta dashed-double-dotted curve represents the power approximation of the plume size as a function of time during diffusive expansion at $p_b = 1$ bar. The inset shows the distributions of the vapor (red solid curve) and mixture (green dashed curve) velocities near the target for $p_b = 0.1$ bar at $t = 16$ μs. The curves in the inset are obtained by multi-pass linear filtering of raw DSMC data. (b), Plume size at the end of initial expansion L_E (red squares), as well as average speeds of initial expansion $V_E = L_E/\tau_E$ (green triangles) and contraction $V_C = (L_E - L_C)/(\tau_C - \tau_E)$ (blue circles) versus p_b at $F_L = 3$ Jcm^{-2}. In panel (b), the symbols correspond to the calculated values, while the curves are drawn only to guide the eye.

plume stopping time τ_E, as well as the duration of the contraction stage, which lasts more than 44 μs at $p_b = 0.01$ bar. The plume stopping distance L_E varies inversely proportionally to the background gas pressure (Fig. 6(b)). The plume stopping time and contraction time determined based on the data from Fig. 6(a) are given in Table 1.

Interestingly, contrary to the plume sizes, L_E and L_C, and corresponding times, τ_E and τ_C, the relative contraction of the plume, L_C/L_E, demonstrates weak dependence on p_b and varies from 0.76 at $p_b = 0.01$ bar to 0.6 at $p_b = 1$ bar. The average plume expansion, $V_E = L_E/\tau_E$, and contraction, $V_C = (L_E - L_C)/(\tau_C - \tau_E)$, speeds (Fig. 6(b)) also only weekly depend on the background gas pressure. This suggests that the sizes L_E and L_C as well as times τ_E and τ_C exhibit practically the same scaling behavior as functions of the background gas pressure. The conclusion on insensitivity of V_E on the background gas pressure is in agreement with the results of simulations of laser-induced plumes performed under the assumption of constant evaporation flux during laser pulse in Ref. [29].

3.4. Scaling of the plume size during diffusive expansion

In a classical diffusion problem, the size of a cloud of minor admixture diffusing through major species is expected to increase as $t^{1/2}$. This scaling law holds in continuum gas flows, when the molar fraction of admixture is negligibly small, the binary diffusion coefficient is constant, pressure is homogeneous, and bulk mixture velocity is zero. These assumptions are not exactly satisfied during the diffusive stage of the laser-induced plume expansion process.

Table 1
Plume stopping time τ_E, contraction time τ_C, and ratios of τ_E and τ_C to the half-deposition time τ_D, Eq. (13), calculated at $F_L = 3$ Jcm^{-2} and various background gas pressures p_b.

p_b (bar)	0.01	0.1	1
τ_E (μs)	40	4.4	0.455
τ_C (μs)	86	8.9	1.03
τ_E/τ_D	0.74	0.76	0.78
τ_C/τ_D	1.59	1.54	1.78

The results of the DSMC simulations show that, at the diffusive stage of expansion, the plume size scales with time according to the power scaling law

$$\frac{L_{P,E}(t)}{L_C} \propto \left(\frac{t}{\tau_C}\right)^{\beta}. \quad (12)$$

For $F_L = 3$ Jcm^{-2} and $p_b = 1$ bar, such a scaling law is shown in Fig. 6 (a) by the dashed-double-dotted curve. The exponent β, however, is found to be significantly smaller than 1/2. The least-square fitting of the values of $L_{P,E}(t)$ at $t > \tau_C$ results in $\beta = 0.34$ at $p_b = 1$ bar and $\beta = 0.24$ at $p_b = 0.1$ bar. The obtained results are insufficient to reliably determine β at $p_b = 0.01$ bar.

The analysis of the computational results suggests that the major

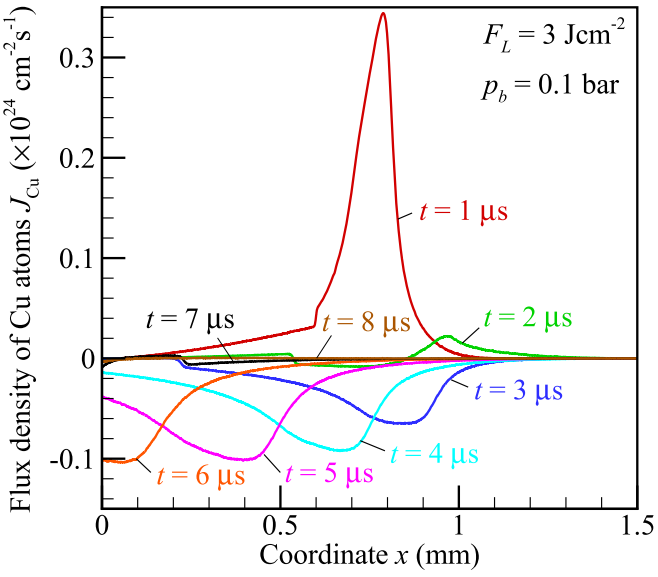

Fig. 7. Distributions of the number flux density $J_{Cu} = n_{Cu}u_{Cu}$ of Cu vapor at various times obtained for $F_L = 3$ Jcm^{-2} and $p_b = 0.1$ bar. The time for each curve is indicated in the figure panel.

factor resulting in the deviation of β from the expected value of 1/2 is the continuing deposition of vapor back to the irradiated surface during the diffusive expansion. Due to vapor redeposition, the vapor velocity at the surface remains relatively large and directed towards the surface during the diffusive expansion. For example, at $F_L = 3$ Jcm^{-2} and $p_b = 0.1$ bar, the vapor velocity at the surface is equal to ~180 ms^{-1} at a time of 16 μs. The distributions of the vapor and mixture velocities under these conditions are shown in the inset of Fig. 6(a), although the vapor velocity in the close vicinity of the surface is out of the velocity range considered in this plot. As one can see, the gas mixture velocity remains negative inside the plume and has the same order of magnitude as the diffusion velocity of vapor. Thus, the presence of the surface with the boundary conditions, which enable the continuous redeposition of vapor and induce the bulk flow towards the irradiated surface, reduces the overall rate of the diffusive plume growth compared to the rate expected for diffusion of a free vapor cloud in a background gas.

3.5. Delayed material redeposition

During the plume contraction, a strong flow directed towards the irradiated surface is developed in the plume. This is illustrated in Fig. 7, where the distribution of the vapor number density flux $J_{Cu} = n_{Cu}u_{Cu}$ (n_{Cu} and u_{Cu} are the number density and bulk velocity of vapor) are plotted for $F_L = 3$ Jcm^{-2} and $p_b = 0.1$ bar. At contraction, J_{Cu} becomes negative practically everywhere in the plume, with exception of a region between the surface and the secondary shock, where J_{Cu} is practically equal to zero. This backward flow is unexpectedly strong: The typical absolute value of J_{Cu} during the contraction stage is only a few times smaller than the maximum absolute value of J_{Cu} during initial expansion. Although the backflow of vapor is induced by the propagation of the secondary shock wave, the maximum magnitude of the back flux is developed well behind the secondary shock wave. The point of maximum of $|J_{Cu}|$ reaches the surface at a time of ~ 6 μs, when the strong redeposition of the ablated material back to the irradiated surface starts. Due to the redeposition, the magnitudes of both velocity and density decrease fast at a later time. Although the reflected shock wave is visible in the distribution of J_{Cu} obtained at $t = 7$ μs, already at $t = 8$ μm the flux becomes practically equal to zero everywhere in the plume. The later diffusive expansion of the plume illustrated in Fig. 2(c) occurs under conditions of nearly zero bulk velocity, when the gas mixture velocity inside the plume is about 10–20 ms^{-1}, e.g., see inset in Fig. 6(a).

To characterize the dynamics of the material redeposition, the total vapor contents of the plume N_{Cu}, Eq. (10), is plotted versus time in Fig. 8 (a)-(d) for various laser fluences and background gas pressures. In all simulations, the vapor atoms do not reach the external boundary of the computational domain, so N_{Cu} varies with time only due to evaporation and condensation processes at the irradiated surface.

At the smallest fluence of 1.5 Jcm^{-2}, the redeposition starts almost immediately after the laser pulse. The onset of the backflow-related redeposition right after the termination of the laser pulse can also occur at larger fluences if the background gas pressure is sufficiently large, e.g., at $F_L = 2$ Jcm^{-2} and $p_b = 1$ bar. With increasing fluence or

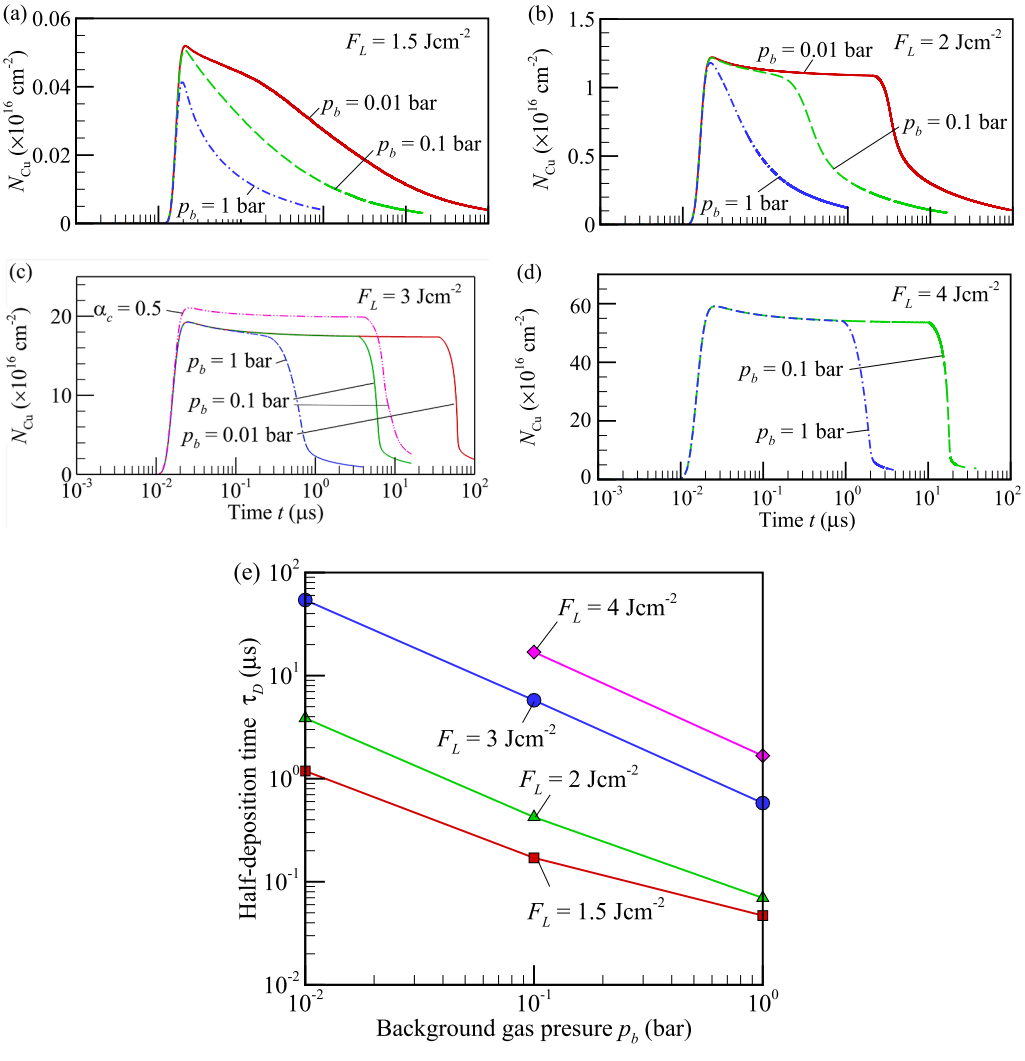

Fig. 8. Total number N_{Cu} of Cu atoms in the plume per unit cross-sectional area versus time t obtained for a laser fluence of $F_L = 1.5$ Jcm^{-2} (a), 2 Jcm^{-2} (b), 3 Jcm^{-2} (c), and 4 Jcm^{-2} (d) at a background gas pressure of $p_b = 0.01$ bar (red solid curves), 0.1 bar (green dashed curves), and 1 bar (blue dashed-dotted curves). Panel (e) shows the half-deposition time τ_D defined by Eq. (13) versus background gas pressure p_b at $F_L = 1.5$ Jcm^{-2} (red squares), 2 Jcm^{-2} (green triangles), 3 Jcm^{-2} (blue circles), and 4 Jcm^{-2} (magenta diamonds). In panel (c), the magenta dashed-double-dotted curve is obtained at $\alpha_c = 0.5$ at $p_b = 0.1$ bar, while other data correspond to $\alpha_c = 0$. In panel (e), the symbols correspond to the calculated values, while the curves are drawn only to guide the eye.

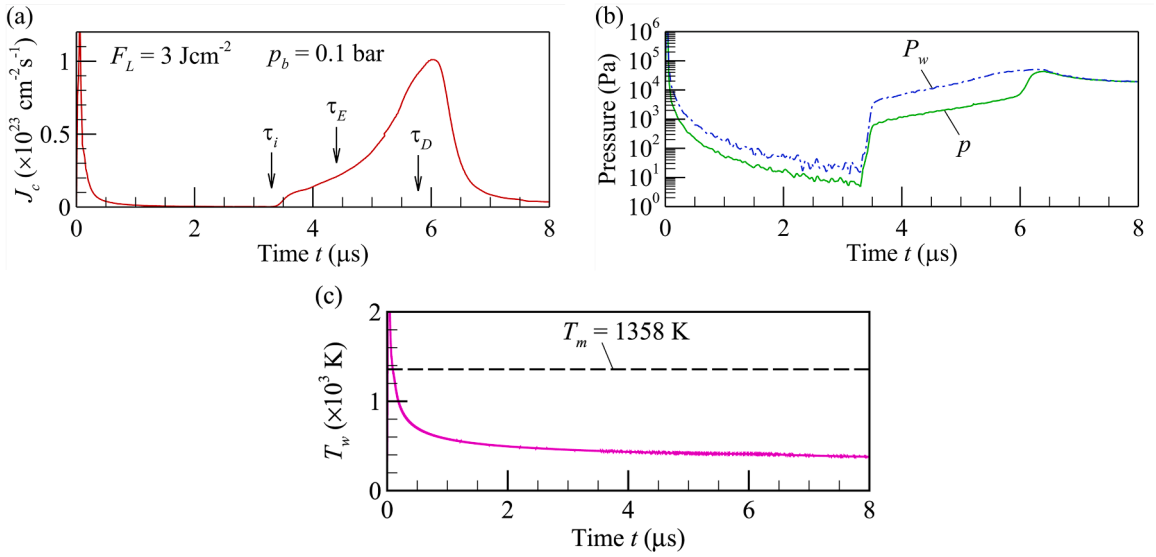

Fig. 9. Condensation number flux density J_c [a, Eq. (2)], pressure at the surface (b), and surface temperature of the irradiated target T_w (c) versus time t at a laser fluence of $F_L = 3$ Jcm^{-2} and background gas pressures of $p_b = 0.1$ bar. In panel (a), the vertical arrows indicate the time of arrival of the internal shock wave on the surface τ_i, plume stopping time τ_E, and half-deposition time τ_D. In panel (b), the green solid and blue dashed-dotted curves correspond to the pressure in a cell nearest to the surface p and net linear momentum flux density P_w of all plume particles, including the vapor and background gas, Eq. (14), crossing the target surface, respectively. The background gas provides significant contributions to p and P_w only at $t > 6$ μs. In panel (c), the dashed line corresponds to the melting temperature T_m of copper.

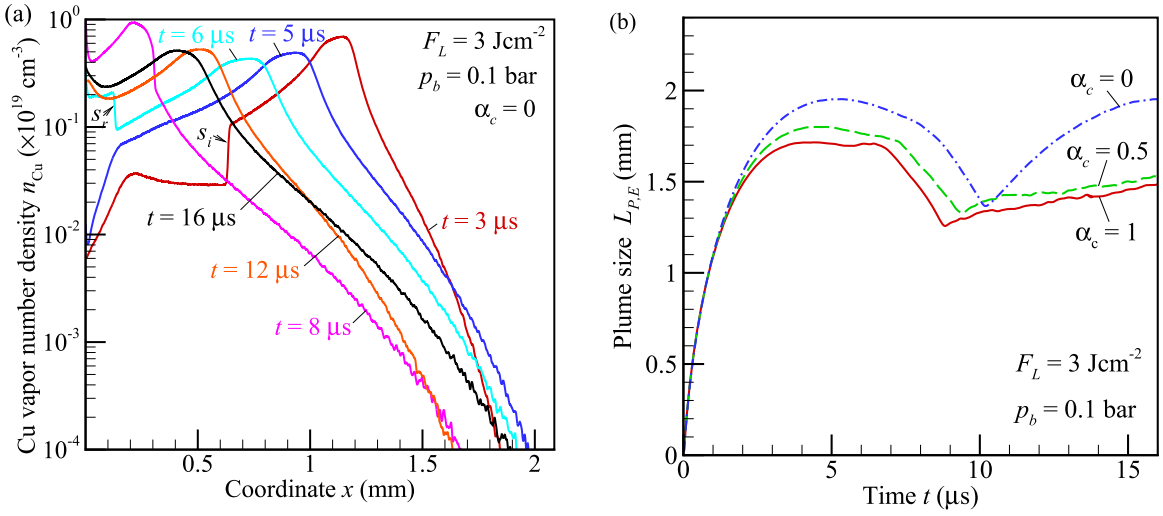

Fig. 10. (a), Distributions of the number density n_{Cu} of Cu vapor at various times obtained for a laser fluence of $F_L = 3$ Jcm^{-2}, background gas pressures of $p_b = 0.1$ bar, and condensation coefficient α_c equal to zero. s_i and s_r mark the positions of the internal (secondary) and reflected shock waves, respectively. The time for each curve is indicated in the figure panel. (b), Plume size $L_{P,E}$ versus time obtained at $F_L = 3$ Jcm^{-2} and $p_b = 0.1$ bar when $\alpha_c = 1$ (red solid curve), 0.5 (green dashed curve), and 0 (blue dashed-dotted curve).

decreasing background gas pressure, the processes of strong evaporation and material redeposition are separated by a relatively long time interval, when N_{Cu} is nearly constant and only slowly decreases due to condensation as predicted by the Knudsen layer theory [45]. The strong redeposition starts in this case close to the end of the contraction stage and terminates at $t \sim \tau_C$. During this delayed redeposition process, typically about 90% of the evaporated material condensate at the surface.

Thus, in the 1D long-term plume expansion processes, the absolute majority of the evaporated material condensates back to the irradiated target. This strong redeposition effect is not related to the slow condensation in the Knudsen layer but originates from the propagation of the internal shock wave, which induces the backflow and plume contraction. The processes of plume contraction and strong material redeposition are mutually connected as they both are induced by the internal shock wave.

The delayed redeposition terminates some time before the termination of the plume contraction. After the end of strong redeposition, the weak redeposition proceeds during the remaining duration of the contraction stage and subsequent diffusive expansion. Since the process of deposition is continuous, the current simulations do not allow us to find the total fraction of the condensed material or determine a nominal time when the condensation is terminated. To characterize the time scale of the redeposition process, therefore, one can introduce the half-deposition time τ_D, which is equal to a time, when a half of the maximum amount of vapor particles deposits back to the irradiated surface, i.e.,

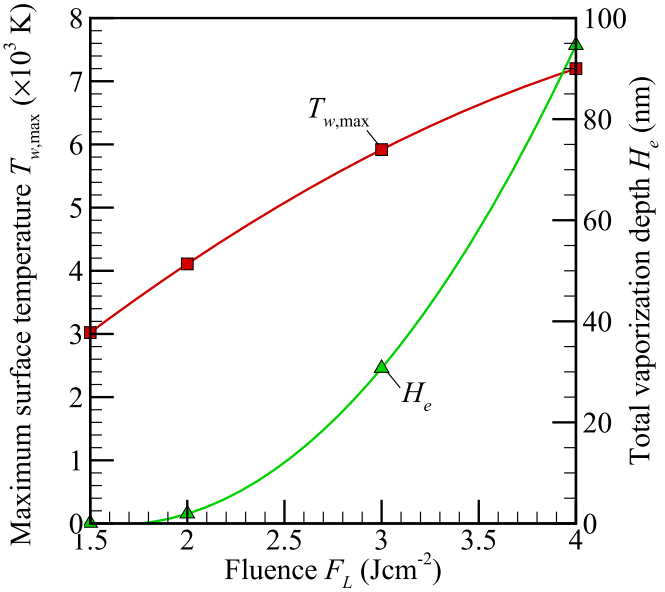

Fig. 11. Maximum surface temperature $T_{w,\max}$ (red squares) and total vaporization depth H_e [green triangles; Eq. (A.9)] versus laser fluence F_L obtained at a background gas pressure of 0.1 bar. The symbols are obtained in simulations, while the curves are drawn only to guide the eye.

$$N_{\mathrm{Cu}}(\tau_D) = \frac{\max\{N_{\mathrm{Cu}}(t)\}}{2}. \tag{13}$$

The values of τ_D are shown in Fig. 8(e). In cases, when the strong redeposition is separated from evaporation by a long time delay, e.g., at $F_L = 3$ Jcm^{-2}, τ_D varies inversely proportionally to the background gas pressure: $\tau_D \propto 1/p_b$. The ratios of the plume stopping time τ_E and contraction time τ_C to the half-deposition time τ_D, however, are conservative values and only marginally depend on the background gas pressure if the laser fluence is fixed (Table 1). The calculated values of $\tau_E/\tau_D \sim 0.75$ and $\tau_C/\tau_D \sim 1.6$ confirm that most of vapor condensates at the surface during the later stage of plume contraction. The half-deposition time roughly corresponds to the time when the condensation flux J_c is at maximum (Fig. 9(a)).

The arrival of the internal shock and subsequent material redeposition also produce strong dynamic effect on the irradiated target (Fig. 9 (b)). This effect can be characterized by the gas mixture pressure $p = nRT$ (here, n, R, and T are the gas mixture number density, average gas constant, and temperature) and linear momentum flux density

$$P_w = \int\limits_{v_x<0} v_x^2 m_v f_v(0,\mathbf{v},t)d\mathbf{v} + \int\limits_{v_x<0} v_x^2 m_b f_b(0,\mathbf{v},t)d\mathbf{v} \tag{14}$$

at the target surface. The value of p is different from P_w since the latter accounts for the contibution of bulk velocity of the gas mixture. During initial expansion and contraction of the plume, a low-density zone is formed near the target surface, where the pressure can be orders of magnitude smaller than the background gas pressure. Under conditions illustrated in Fig. 9, the gas pressure at the surface before the arrival of the internal shock is as low as 10 Pa. The formation of similar low-density zone is also observed in two-dimensional simulations of laser-induced plume expansion at finite laser spot sizes [25]. When the internal shock arrives, the pressure at the surface increases in three orders of magnitude and continues to rise during the whole process of delayed material redeposition until a time of ~ 6.4 μs (cf. Fig. 9(a) and (b)). After that, the gas mixture at the surface primary consists of the background gas, and the surface pressure reduces to a level of the background gas pressure p_b. Under conditions considered in Fig. 9, the relatively large pressure associated with the delayed redeposition process, however, cannot stimulate the expulsion of the molten material from the ablation crater since the resolidification process ends long before the arrival of the secondary shock wave, at $t = \sim 0.0935$ μs (Fig. 9(c)).

Table 3
Parameters of the VHS molecular model (molecular diameter d_{ref} at a reference temperature T_{ref} and viscosity index ω) for Ar-Ar, Cu-Cu, and Cu-Ar atom pairs. The values of ω are obtained by least-square fitting of the viscosity calculated in the form of one-term expansions with respect to the Sonine polynomials in the temperature range $T_{f,min} \le T \le T_{f,max}$ based on the MLR interatomic potentials that are established in QMC calculations; then the value of d_{ref} is calculated from Eq. (A.18) to fit the gas viscosity μ_{ref} at T_{ref}. For Cu-Ar atom pair, μ_{ref} corresponds only to the first-order contribution of Cu-Ar collisions to the total gas mixture viscosity [49].

Atom pair	T_{ref} (K)	d_{ref} (Å)	ω	μ_{ref} (μPa s)	$T_{f,min}$ (K)	$T_{f,max}$ (K)
Ar-Ar	$3{\cdot}10^2$	3.929	0.7055	22.65	$3{\cdot}10^2$	10^4
Cu-Cu	$3{\cdot}10^2$	5.446	0.6958	14.74	10^2	10^4
Cu-Ar	$3{\cdot}10^2$	3.955	0.7566	25.98	$3{\cdot}10^2$	10^4

3.6. Effect of the condensation coefficient

To quantify the effect of the condensation coefficient α_c on the long-term dynamics of laser-induced plumes, additional simulations were performed with $\alpha_c = 0$ and 0.5 at $F_L = 3$ Jcm^{-2} and $p_b = 0.1$ bar. These simulations showed that the value of α_c has a multifaceted impact on the plume structure and distributions of plume parameters. Due to reduced or absent condensation, larger vapor density is retained between the surface and internal shock wave. It results in the smaller pressure ratio across this shock wave, smaller speed of the shock, and delayed interaction of the internal shock with the target. It can be seen, e.g., from the comparison of the vapor density distributions shown for $\alpha_c = 0$ and $\alpha_c = 1$ in Figs. 10(a) and 5(b), respectively. The internal shock wave reaches the surface at ~ 3.3 μs for $\alpha_c = 1$ and only at ~ 5 μs for $\alpha_c = 0$. After the reflection of the internal shock, the value of α_c has even stronger effect on the flow during further diffusive expansion. In the flow with no condensation, the vapor density near the irradiated surface remains relatively large during much longer time interval. For example, at $t = 16$ μs, the vapor density near the surface is more than order of magnitude larger at $\alpha_c = 0$ than at $\alpha_c = 1$. The large density near the surface also increases the strength and propagation speed of the reflected shock wave. At the same time, the case of $\alpha_c = 0$ compared to the case of $\alpha_c = 1$ is characterized only by ~15% increase in the plume stopping size L_E and corresponding moderate increases in the stopping time, contraction time, and plume size at the end of contraction (cf. blue dashed-dotted and red solid curves in Fig. 10(b)). In agreement with the previous

Table 2
Parameters of the MLR potentials given by Eq. (A.12)-(A.16) for Ar-Ar, Cu-Cu, and Cu-Ar atom pairs and masses of atoms m_k used in the present work [49]. The masses of atoms are chosen to be equal to standard atomic weights according to the NIST database, https://www.nist.gov/pml/atomic-weights-and-isotopic-compositions-relative-atomic-masses.

Atom pairs	D_e (eV)	r_e (Å)	C_6 (eV Å^6)	C_8 (eV Å^8)	C_{10} (eV Å^{10})	β_0	β_1	β_2	β_3	β_4	m_k (Da)
Ar-Ar	$1.225{\cdot}10^{-2}$	3.770	2.003	−2.815	1.153	$2.785{\cdot}10^{-1}$	−2.602	−3.036	−3.319	−2.453	39.948
Cu-Cu	2.200	2.192	$2.017{\cdot}10^{1}$	$-1.283{\cdot}10^{1}$	2.290	−1.530	−4.766	−5.815	−4.145	−1.491	63.546
Cu-Ar	$1.013{\cdot}10^{-2}$	4.039	$4.194{\cdot}10^{-2}$	$-2.574{\cdot}10^{-1}$	$6.916{\cdot}10^{-1}$	$-2.019{\cdot}10^{-1}$	−6.768	−7.384	−9.995	−6.909	–

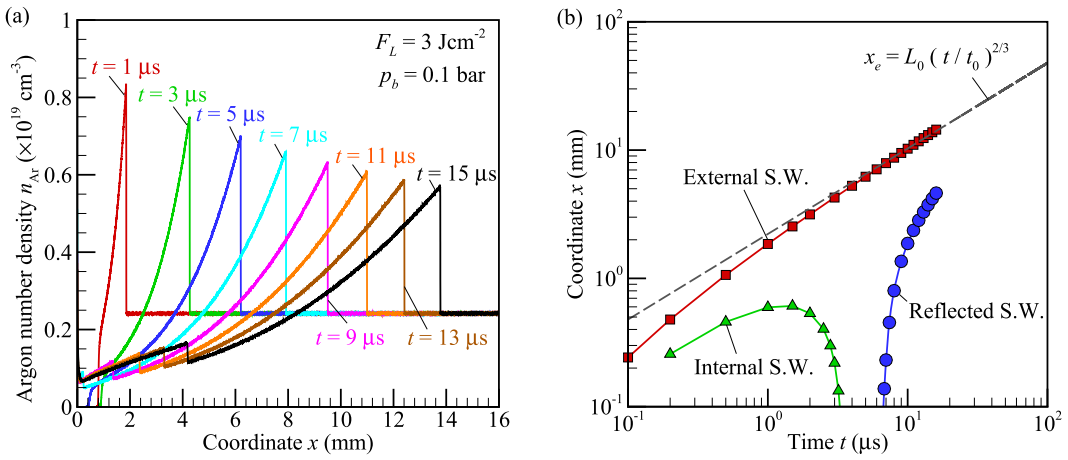

Fig. 12. (a), Distributions of the number density n_{Ar} of Ar background gas at various times obtained for a laser fluence of $F_L = 3$ Jcm^{-2} and background gas pressure of $p_b = 0.1$ bar. The time for each curve is indicated in the figure panel. (b), Positions of the external (red squares), internal (green triangles), and reflected (blue circles) shock waves (S.W.) versus time t in the plume expansion process illustrated in panel (a). In panel (b), the symbols correspond to the data points obtained in simulations, while the solid curves are drawn only to guide the eye; the black dashed curve corresponds to the Sedov-Taylor solution for the planar blast wave, $x_e(t) = L_0(t/t_0)^{2/3}$, where $t_0 = 1$ μs and the value $L_0 = 2.22$ mm is obtained by least-square fitting of calculated positions of the external shock at $t \geq t_0$.

analysis of the density distributions, the strongest difference between variations of the integral plume size versus time in the flows with and without surface condensation is observed during the diffusive expansion, when the plume size grows much faster if $\alpha_c = 0$. This occurs because the reflected shock wave is stronger and moves faster in the case of no condensation. The faster motion of the reflected shock induces larger bulk velocity behind the shock. In this case, the expansion of the plume after the termination of the plume contraction stage is a result of diffusion augmented by the bulk flow in the plume directed from the irradiated target.

The moderate decrease in the condensation coefficient from 1 to 0.5, however, induces only minor changes in the variation of the plume size in time (Fig. 10(b)) and in the dynamics of material redeposition. In particular, this reduction of α_c only marginally affect the amount of vapor condensed at the surface during the rapid condensation at the end of the plume contraction. This can be concluded based on the comparison of the variation of the plume content $N_{Cu}(t)$ obtained for $\alpha_c = 1$ and 0.5 at $F_L = 3$ Jcm^{-2} and $p_b = 0.1$ bar and shown by the dashed-dotted and dashed-double-dotted curves in Fig. 8(c).

3.7. Discussion

The Knudsen layer models [45] and direct kinetic simulations, e.g., [56], predict that the value of the condensation flux of vapor particles returning back to the irradiated surface due to interatomic collisions in the Knudsen layer during strong evaporation is equal to 16–19% of the evaporated flux. This quantity is usually considered as an estimate of the effect of the material redeposition in the laser ablation problem, while condensation in the plume after termination of the laser pulse is often neglected, e.g., [33]. The simulations performed in the present paper show that this estimation is, in fact, incorrect, and the long-term dynamics of one-dimensional plumes is accompanied by unexpectedly strong redeposition of vapor on the irradiated target, where up to 90% of the ablated mass can return to the target surface. Most of vapor redeposits at the surface not during the laser pulse but after a delay with respect to the laser pulse end. During plume contraction, a strong bulk flow directed towards the surface of the irradiated target is developed. This flow augments the redeposition of the ablated material back to irradiated surface. Although a decrease in the background gas pressure can increase the time delay between the pulse and the onset of delayed deposition, the latter occurs under all conditions considered in the simulations.

Contrary to the 1D case considered in the present paper, the radial expansion of the vapor plume from relatively small laser spots would result in the deposition of ablated mass around the ablation crater. The vapor redeposition would occur on a much larger surface area and, therefore, may not effectively change the volume of the ablation crater and laser drilling efficiency. The backflow of redeposited material can either lead to pollution of the machining surface [7] or be used for surface modification [36]. For example, experiments in Ref. [36] indicated a strong redeposition of steel ablated by a 25 ns laser pulse at a fluence of 10 Jcm^{-2} and atmospheric pressure back to irradiated surface on the time scale of tens of μs. The duration of the redeposition process in these experiments agrees on the order of magnitude with the half-deposition time obtained in the present work. Thus, the delayed redeposition of the vapor back to the irradiated surface observed in 1D simulations agrees with the experimental works that reveal massive redeposition of the ablated material around the laser spot.

The simulation results allow one to hypothesize that the redeposition of the ablated material and quality of surface machining or modification may be controlled by engineering an appropriate double-pulse or multipulse burst. In this case, the first pulse in the burst can be used to ablate material, while the second and subsequent pulses can be used not only to ablate additional material but also to manage the redeposition of material ablated by the preceding pulses in the burst. The intra-burst repetition rate, or pulse-to-pulse separation time between pulses in the burst, can be chosen, depending on the purpose of manufacturing, to either destroy the back flow in the plumes induced by the preceding pulses and minimize the pollution of the machining surface or to promote material redeposition at a desired distance from the laser beam and enhance modification of surface morphology. Moreover, the variation of the characteristic deposition time depending on the laser fluence and background gas pressure could enable controllable growth of nanoclusters in the back flow and modifications of the surface with functional nanoparticle coatings.

4. Conclusions

One-dimensional simulations of long-term vapor plume expansion into a background gas induced by irradiation of a material target with a nanosecond laser pulse show that the initial stage of initial intertial expansion and subsequent stage of diffusive expansion are separated by a relatively long contraction stage, when the integral size of the plume exhibits 30–50% reduction. At the end of the contraction stage, the ablated material experiences unexpectedly strong deposition back to the irradiated surface. During this redeposition process, up to 90% of the

initially vaporized material can be condensed back at the irradiated surface. Both plume contraction and rapid condensation are induced by the propagation of the internal shock wave and strong backflow developed in the plume behind this shock. Thus, the observed delayed condensation at the irradiated targed is augmented by the bulk flow directed towards the surface. During this delayed condensation, a pressure buildup is developed at the irradiated surface. The moderate variation of the vapor condensation coefficient at the irradiated surface does not change this picture qualitatively and induces only small-to-moderate quantitative changes in the durations of individual expansion stages as well as in the total amount of vapor condensed at the surface.

To quantify the duration of each expansion stage, a few measures of the plume size are introduced. Since the surface condensation speed and diffusion speed of vapor are of the same order of magnitude, the laser plume size during the diffusive expansion increases slower than expected from a classical diffusion problem due to continuing condensation of vapor at the surface. The major linear and length scales that characterize the size of the plume and duration of the expansion process at the end of initial inertial expansion and contraction are calculated and presented in the reduced form, e.g., in the form of a ratio of the plume stopping time to the plume contraction time. The simulation results show that these ratios are weakly dependent on the background gas pressure and can be considered only as functions of the laser pulse fluence and duration.

The simulations performed in a range of laser fluence and background gas pressure show that strong contraction and almost complete condensation of vapor at the irradiated target are ubiquitous for one-dimensional planar plume expansion. The obtained results, however, are directly applicable only to the case of large laser spot sizes, when the effect of the radial expansion of the plume can be neglected during the considered process time. Nevertheless, the simulation results suggest that the long-term dynamics of laser-induced plume could play a key role in multipulse laser processing, especially at high-repetition rates when the pulse-to-pulse separation is on the same timescale as the characteristic time of plume contraction.

The redeposition of material during the long-term expansion of plumes can also change the target surface morphology. In burst laser ablation, the modulation of the intra-burst repetition rate could potentially allow one to prevent redeposition of ablated material or to control this process for proper surface modification.

In the high-power nanosecond laser ablation, the ablation plume may also contain nanoparticles and droplets which are formed as a result of melt expulsion from the ablation crater and explosive fragmentation [46,57] of the target material as well as condensation of vapor during the contraction and diffusion stages. The coupling of the nanoparticles and vapor phase, interaction of nanoparticles with multiple shock waves, propagating inside the plume, as well as scattering and attenuation of laser radiation on nanoparticles can result in transient changes in plume density distribution and further affect the processes of plume contraction and material redeposition.

Therefore, further quantification of the effect of plume contraction and material redeposition under conditions of finite laser spots, multipulse irradiation, and plume heterogeneity is necessary.

CRediT authorship contribution statement

Alexey N. Volkov: Conceptualization, Data curation, Methodology, Formal analysis, Investigation, Software, Visualization, Supervision, Writing – original draft, Writing – review & editing. **Zhibin Lin:** Methodology, Validation, Writing – original draft, Writing – review & editing.

Declaration of Competing Interest

The authors declare that they have no known competing financial interests or personal relationships that could have appeared to influence the work reported in this paper.

Data availability

Data will be made available on request.

Acknowledgments

This work was supported by MKS Instruments, Inc. A.N.V. also acknowledges support from NSF through RII-Track-1 Future Technologies and Enabling Plasma Processes project (award OIA-2148653).

Appendix A. Thermal model of the irradiated target

The thermal model of the irradiated target predicts the temperature distribution inside the target material. The target temperature field $T_t(t,\xi)$ is described in a moving frame of reference with the coordinate $\xi = x - X_w(t)$, where t is the time, x is the coordinate in the laboratory frame of reference, counting along the normal to the irradiated surface from the point $x = 0$ that corresponds to the initial position of the surface at $t = 0$, and the interface function $X_w(t)$ is equal to the coordinate x of the surface at time t. The temperature field $T_t(t,\xi)$ is determined by the 1D unsteady heat conduction equation that can be written as follows

$$\rho_t[c_t + L_m\delta(T_t - T_m)]\left(\frac{\partial T_t}{\partial t} + V_w\frac{\partial T_t}{\partial \xi}\right) = \frac{\partial}{\partial \xi}\left(\kappa_t\frac{\partial T_t}{\partial \xi}\right) + (1-R_t)\alpha_t I_L(t)\exp(-\alpha_t|\xi|), \tag{A.1}$$

where c_t, ρ_t, κ_t, α_t, R_t, L_m, and T_m are the specific heat, density, thermal conductivity, linear absorption coefficient, reflectivity, latent heat of melting, and melting temperature of the target material, V_w is the velocity of surface recession due to the net effect of evaporation and condensation (V_w is positive, if the net effect is evaporation), $I_L(t)$ is the intensity of laser radiation incident to the target, and $\delta(T)$ is the Dirac delta function. The term $L_m\delta(T_t - T_m)$ in Eq. (A.1) accounts for the energy required to melt or re-solidify the target material in the framework of the enthalpy formulation approach [58,59]. The last term on the right-hand side of Eq. (A.1) describes the absorption of laser radiation according to Beer's law. The local values of material properties c_t, ρ_t, and κ_t in Eq. (A.1), are calculated as functions of temperature by interpolating constant values specific for solid and liquid material as described in Ref. [9].

Eq. (A.1) is solved together with the equation for the interface function:

$$\frac{dX_w}{dt} = -V_w. \tag{A.2}$$

The interface velocity V_w is defined by the number flux densities of atoms that evaporate from, J_e, and condense at, J_c, the irradiated surface:

$$V_w = m_v \frac{J_e - J_c}{\rho_t}. \tag{A.3}$$

The evaporation flux density J_e is calculated based on the Hertz-Knudsen model [45], assuming that the evaporation coefficient is equal to 1 and the velocity distribution function of atoms evaporated from the surface is determined by Eq. (1):

$$J_e = \frac{p_v(T_w)}{m_v\sqrt{2\pi(k_B/m_v)T_w}}. \tag{A4}$$

Here, $p_v(T)$ is the saturated vapor pressure at temperature T, and $T_w = T_t(t,0)$ is the surface temperature. The equilibrium vapor pressure $p_v(T)$ is determined by the Clausius-Clapeyron equation

$$p_v(T) = p_{v,0}\exp\left[\frac{L_v}{k_B/m_v}\left(\frac{1}{T_{v,0}} - \frac{1}{T}\right)\right], \tag{A.5}$$

where L_v is the latent heat of boiling, and $T_{v,0}$ is the boiling temperature at a pressure $p_{v,0}$. The condensation flux density J_c is determined by the kinetic model of plume expansion, Eq. (2).

Eq. (A.1) is solved in a domain of finite size H_t (Fig. 1). At the initial time $t = 0$, the target is assumed to have a uniform temperature T_0, so that Eq. (A.1) and (A.2) are solved with the initial conditions:

$$\text{At } t = 0: \ T_t(0,\xi) = T_0, \ X_w(0) = 0. \tag{A.6}$$

At the irradiated surface where $\xi = 0$, the boundary conditions for Eq. (A.1) represent an energy balance equation:

$$\text{At } \xi = 0: \ L_v\rho_t V_w = -\kappa_t\frac{\partial T_t}{\partial \xi}. \tag{A.7}$$

The value of H_t is assumed to be sufficiently large, so that the variation of temperature at this boundary can be neglected during the whole process under consideration. Then the lower boundary of the computational domain at $\xi = -H_t$ can be assumed to be isothermal and kept at the initial target temperature T_0:

$$\text{At } \xi = -H_t: \ T_t(t,-H_t) = T_0. \tag{A.8}$$

The values of the maximum surface temperature $T_{w,\max}$ and total vaporization depth

$$H_e = \frac{m_v}{\rho_t}\int_0^\infty J_e(t)dt \tag{A.9}$$

obtained with the present model for a Cu target as functions of the laser fluence F_L are shown in Fig. 11. These values are obtained in hybrid simulations of laser ablation with parameters described in Section 2.2 at $p_b = 0.1$ bar, however, $T_{w,\max}$ and H_e only marginally depend on p_b due to the effect of the condensation flux J_c on V_w in Eq. (A.3). The time-dependent variations of T_w, J_e, and J_c under irradiation conditions considered in the present work can be found in Ref. [48].

Appendix B. Sampling of binary collisions based on *ab initio* interatomic potentials

Sampling of binary collisions in the DSMC method is performed based on the solution of the classical elastic scattering problem for point mass particles, e.g., [43,49]. In this problem, the deflection angle χ (angle between the relative velocity vectors of colliding particles before and after a collision) is calculated as a function of the magnitude of the relative particle speed before the collision C_r and geometrical collision parameter b:

$$\chi(C_r,b) = \pi - \int_{r_{min}}^\infty \frac{L_r dr}{mr^2\sqrt{\frac{H_r - V(r)}{2m} - \frac{L_r^2}{(2mr)^2}}}, \tag{A.10}$$

where r is the interatomic distance, $m = m_1m_2/(m_1+m_2)$ is the reduced mass for interacting particles with masses m_1 and m_2 (Table 2), $V(r)$ is the pair interatomic potential, $H_r = mC_r^2/2$, $L_r = mC_rb$, and r_{min} is the minimum distance between particles attained at a collision which can be found as the largest root of the equation

$$\frac{H_r - V(r_{min})}{2m} = \frac{L_r^2}{(2mr_{min})^2}. \tag{A.11}$$

In the present work, $V(r)$ is represented in the form of the Morse longe range (MLR) potential [60]

$$V(r) = D_e\left(1 - \frac{u(r)}{u(r_e)}e^{-\beta(r)y(r)}\right)^2 - D_e, \tag{A.12}$$

where

$$u(r) = \frac{C_6}{r^6} + \frac{C_8}{r^8} + \frac{C_{10}}{r^{10}}, \tag{A.13}$$

$$\beta(r) = y(r)\,\beta_\infty + [1 - y(r)] \sum_{i=0}^{4} \beta_i y(r)^i, \tag{A.14}$$

$$y(r) = \frac{r^3 - r_e^3}{r^3 + r_e^3}, \tag{A.15}$$

$$\beta_\infty = \ln \frac{2D_e}{u(r_e)}. \tag{A.16}$$

The parameters of the MLR potentials (Table 2) for Ar-Ar, Cu-Cu, and Cu-Ar atom pairs were determined in Ref. [49] by least square fitting of the potential energy curves obtained in *ab initio* QMC calculations.

Eq. (A.10) is used to tabulate the dependence $\chi = \chi(b, C_r)$ in the range $0 \le b \le b_{max}$ and $0 < C_r \le C_{r,max}$ on a mesh with equal spacings $\Delta b = 0.02$ Å and $\Delta C_r = 10$ ms^{-1}, where $b_{max} = 20$ Å and $C_r = 12$ kms^{-1}. The total number of collisions in a cell of the computational mesh at a time step was calculated using the NTC collision sampling scheme [43] based on the total collision cross section πb_{max}^2. For each atom pair with a relative speed C_r, which is picked up for collision, the random value of the b is calculated as $b = b_{\max}\sqrt{\eta}$ (here η is a random number homogeneously distributed between 0 and 1) and used to find χ from the look-up table for corresponding pair of species. Then the random azimuth angle $\varepsilon = 2\pi\eta$ is calculated, and the values of χ and ε are used to determine the post-collisional velocities of particles based on the equations that can be found in Ref. [43].

The viscosities of Ar gas, Cu vapor, and Ar-Cu gaseous mixture in a broad range of temperature were calculated based on the present model of interatomic collisions in Ref. [49] using the one- and ten-terms expansions with respect to the Sonine polynomials of the Chapman-Enskog method. The obtained non-power-law dependencies of viscosity on temperature can be approximated by the variable hard sphere (VHS) molecular model, which result in the power dependences of viscosity μ of pure substances on temperature [43]:

$$\mu = \mu_{ref} \left(\frac{T}{T_{ref}} \right)^{\omega}, \tag{A.17}$$

where

$$\mu_{ref} = \frac{15m}{(5 - 2\omega)(7 - 2\omega) d_{ref}^2} \sqrt{\frac{k_B T_{ref}}{2\pi m}}, \tag{A.18}$$

d_{ref} is the reference molecular diameter at a reference temperature T_{ref}, and ω is the viscosity index. The parameters of the VHS models that are determined by fitting the viscosity data obtained in Ref. [49] using the MLR potentials for Ar-Ar, Cu-Cu, and Ar-Cu atom pairs are provided in Table 3.

Appendix C. Propagation of the external, internal, and reflected shock waves

The distributions of Ar background gas number density obtained at $F_L = 3$ Jcm^{-2} and $p_b = 0.1$ bar are shown in Fig. 12(a). These distributions, together with the corresponding distributions of the gas mixture density, allow one to calculate the positions of the external, internal, and reflected shock waves (Fig. 12(b)).

After some initial expansion time, the position $x_e(t)$ of the external shock wave can be approximated by the Sedov-Taylor solution for the planar blast wave, $x_e(t) = L_0(t/t_0)^{2/3}$ [61]. Such an approximation, where $t_0 = 1$ μs and parameter $L_0 = 2.22$ mm is obtained by least-square fitting of calculated positions of the external shock at $t > t_0$, is shown in Fig. 12(b) by the dashed curve. A reasonable agreement between the blast wave theory and results of direct 1D [29] and two-dimensional [62] simulations of laser-induced plumes has been previously demonstrated. It is worth noting that such an agreement is expected only in a limited range of the expansion time, $t_1 < t < t_2$. At the initial stage of expansion, $t < t_1$, the propagation of the external shock does not correspond to the Sedov-Taylor solution because the distributions of flow parameters between the shock and mixing layer do not closely resemble the distributions in the expansion from a point source. At longer times, $t > t_2$, the propagation of the external shock deviates from the Sedov-Taylor solution due to increasing dissipation effects, as well as interaction with the reflected shock that moves faster than the primary one. The latter is apparent from the shock wave trajectories shown in Fig. 12(b).

The experimental studies of expansion dynamics of laser-induced plumes, e.g., [12,13,63-68] demonstrate a relatively good agreement between the blast wave theory and experimentally measured positions of the plume boundary only during short initial time, $t <\sim 1$ μs, and at small background gas pressures, ~ 1 Torr. In these experimental studies, however, the measured position corresponds to the boundary of the luminous plasma plume. It is not surprising then that the agreement is observed only at small pressures and short times, when the external shock wave is relatively close to the external boundary of the plume. At larger background gas pressures, the external shock wave moves faster than the plume boundary and runs away from the plume as seen from the comparison of the vapor and background gas density distributions in Figs. 2 and 12(a). In Ref. [14], where the trajectory of the shock wave was obtained by analyzing the experimental shadowgraphs, a good agreement between the theoretical blast wave solution and measurements was established for the initial 2.5 μs of the expansion process induced by ablation of Al target into 1 atm Ar.

Once appeared, the internal shock wave moves from the surface and reaches the maximum distance of ~ 0.61 mm at a time of ~ 1.5 μs. After that it starts to move towards the surface and falls on it at a time of ~ 3.3 μs. The fall of the internals shock does not induce the immediate formation of the reflected shock since $\alpha_c = 1$ in Fig. 12 and the vapor flux incident to the surface completely condenses. The back flow of the background gas reaches the surface with a delay with respect to the internals shock and induces the formation of the reflected shock at a time of ~ 6.7 μs.

References

[1] N.B. Dahotre, S.P. Harimkar, Laser Fabrication and Machining of Materials, Springer, New York, 2008.
[2] P.R. Willmott, J.R. Huber, Pulsed laser vaporization and deposition, Rev. Mod. Phys 72 (2000) 315–328.
[3] D.W. Hahn, N. Omenetto, Laser-induced breakdown spectroscopy (LIBS), part I: review of basic diagnostics and plasma—particle interactions: still-challenging issues within the analytical plasma community, Appl. Spectrosc. 64 (2010) 335A–366A.
[4] J.M. Vadillo, J.M. Fernández Romero, C. Rodríguez, J.J. Laserna, Effect of plasma shielding on laser ablation rate of pure metals at reduced pressure, Surf. Interface Anal. 27 (1999) 1009–1015.
[5] N.M. Bulgakova, A.B. Evtushenko, Y.G. Shukhov, S.I. Kudryashov, A.V. Bulgakov, Role of laser-induced plasma in ultradeep drilling of materials by nanosecond laser pulses, Appl. Surf. Sci. 257 (2011) 10876–10882.
[6] B.S. Yilbas, S.B. Mansoor, Laser evaporative heating of surface: simulation of flow field in the laser produced cavity, J. Phys. D: Appl. Phys. 39 (2006) 3863–3875.
[7] S. Singh, M. Argument, Y.Y. Tsui, R. Fedosejevs, Effect of ambient air pressure on debris redeposition during laser ablation of glass, J. Appl. Phys. 98 (2005), 113520.
[8] J.R. Lawrence (Ed.), Advances in Laser Materials Processing, 2nd ed, Elsevier, Cambridge, 2017.
[9] O.A. Ranjbar, Z. Lin, A.N. Volkov, One-dimensional kinetic simulations of plume expansion induced by multi-pulse laser irradiation in the burst mode at 266 nm wavelength, Vacuum 157 (2018) 361–375.
[10] O.A. Ranjbar, Z. Lin, A.N. Volkov, Effect of the spot size on ionization and degree of plasma shielding in plumes induced by irradiation of a copper target by multiple short laser pulses, Appl. Phys. A 126 (2020) 355.
[11] T.E. Itina, J. Hermann, P. Delaporte, M. Sentis, Laser-generated plasma plume expansion: combined continuous-microscopic modeling, Phys. Rev. E 66 (2002), 066406.
[12] S. Mahmood, R.S. Rawat, M. Zakaullah, J.J. Lin, S.V. Springham, T.L. Tan, P. Lee, Investigation of plume expansion dynamics and estimation of ablation parameters of laser ablated Fe plasma, J. Phys. D: Appl. Phys. 42 (2009), 135504.
[13] S.S. Harilal, C.V. Bindhu, M.S. Tillack, F. Najmabadi, A.C. Gaeris, Internal structure and expansion dynamics of laser ablation plumes into ambient gases, J. Appl. Phys. 93 (2003) 2380–2388.
[14] S.S. Harilal, G.V. Miloshevsky, P.K. Diwakar, N.L. LaHaye, A. Hassanein, Experimental and computational study of complex shockwave dynamics in laser ablation plumes in argon atmosphere, Phys. Plasma. 19 (2012), 083504.
[15] X. Li, W. Wei, J. Wu, S. Jia, A. Qiu, The Influence of spot size on the expansion dynamics of nanosecond-laser-produced copper plasmas in atmosphere, J. Appl. Phys. 113 (2013), 243304.
[16] A.V. Bulgakov, N.M. Bulgakova, Dynamics of laser-induced plume expansion into an ambient gas during film deposition, J. Phys. D: Appl. Phys. 28 (1995) 1710–1718.
[17] J.R. Ho, C.P. Grigoropoulos, J.A.C. Humphrey, Gas dynamics and radiation heat transfer in the vapor plume produced by pulsed laser irradiation of aluminum, J. Appl. Phys. 79 (1996) 7205–7215.
[18] T.E. Itina, W. Marine, M. Autric, Mathematical modelling of pulsed laser ablated flows, Appl. Surf. Sci. 154-155 (2000) 60–65.
[19] A.V. Gusarov, A.G. Gnedovets, I. Smurov, Two-dimensional gas-dynamic model of laser ablation in an ambient gas, Appl. Surf. Sci. 154–155 (2000) 66–72.
[20] Z. Chen, A. Bogaerts, Laser ablation of Cu and plume expansion into 1 atm ambient gas, J. Appl. Phys. 97 (2005), 063305.
[21] V.I. Mazhukin, V.V. Nossov, I. Smurov, Modeling of plasma-controlled evaporation and surface condensation of Al induced by 1.06 and 0.248 μm laser radiations, J. Appl. Phys. 101 (2007), 024922.
[22] S.B. Harris, J.H. Paiste, T.J. Holdsworth, R.R. Arslanbekov, R.P. Camata, Laser-generated plasmas in length scales relevant for thin film growth and processing: simulation and experiment, J. Phys. D: Appl. Phys. 53 (2019), 015203.
[23] D. Sibold, H.M. Urbassek, Kinetic study of pulsed desorption flows into vacuum, Phys. Rev. A 43 (1991) 6722–6734.
[24] T.E. Itina, A.A. Katassonov, W. Marine, M. Autric, Numerical study of the role of a background gas and system geometry in pulsed laser deposition, J. Appl. Phys. 83 (1998) 6050–6054.
[25] A.N. Volkov, G.M. O'Connor, T.J. Glynn, G.A. Lukyanov, Expansion of a laser plume from a silicon wafer in a wide range of ambient gas pressures, Appl. Phys. A 92 (2008) 927–932.
[26] O.A. Ranjbar, Z. Lin, A.N. Volkov, Plume accumulation effect and interaction of plumes induced by irradiation of a copper target with a burst of nanosecond laser pulses near the ionization threshold, J. Appl. Phys. 127 (2020), 223105.
[27] M. Stokes, O.A. Ranjbar, Z. Lin, A.N. Volkov, Expansion dynamics and radiation absorption in plumes induced by irradiation of a copper target by single and multiple nanosecond laser pulses in the doughnut beam mode, Spectrochim. Acta Part B 177 (2021), 106046.
[28] A.N. Volkov, Splitting of laser-induced neutral and plasma plumes: hydrodynamic origin of bimodal distributions of vapor density and plasma emission intensity, J. Phys. D: Appl. Phys. 54 (2021) 37LT01.
[29] A.A. Morozov, V.A. Titarev, Dynamics of planar gas expansion during nanosecond laser evaporation into a low-pressure background gas, Phys. Fluids 34 (2022), 096101.
[30] N. Humphrey, A.N. Volkov, Hydrodynamic splitting of laser-induced plasma plumes: two-dimensional kinetic simulations, Appl. Phys. A 128 (2022) 684.
[31] K.P. Stanyukovich, Unsteady Motion of Continuous Media, Pergamon, New York, 1960.
[32] D. Sibold, H.M. Urbassek, Gas-dynamic study of pulsed desorption flows into a vacuum, Phys. Fluids A: Fluid Dynam. 4 (1992) 165–177.
[33] N. Arnold, J. Gruber, J. Heitz, Spherical expansion of the vapor plume into ambient gas: an analytical model, Appl. Phys. A 69 (1999) S87–S93.
[34] M. Mahjouri-Samani, M. Tian, A.A. Puretzky, M. Chi, K. Wang, G. Duscher, C. M. Rouleau, G. Eres, M. Yoon, J. Lasseter, K. Xiao, D.B. Geohegan, Nonequilibrium synthesis of TiO_2 nanoparticle "building blocks" for crystal growth by sequential attachment in pulsed laser deposition, Nano Lett. 17 (2017) 4624–4633.
[35] A. Ojeda-G-P, M. Döbeli, T. Lippert, Influence of plume properties on thin film composition in pulsed laser deposition, Adv. Mater. Interfaces 5 (2018), 1701062.
[36] A. Pereira, P. Delaporte, M. Sentis, W. Marine, A.L. Thomann, C. Boulmer-Leborgne, Optical and morphological investigation of backward-deposited layer induced by laser ablation of steel in ambient air, J. Appl. Phys. 98 (2005), 064902.
[37] P.M. Ossi, Cluster synthesis and cluster-assembled film deposition in nanosecond pulsed laser ablation, in: A. Miotello, P.M. Ossi (Eds.), Laser-Surface Interactions for New Materials Production, Springer, New York, 2010, pp. 99–124.
[38] B. Tan, Deep micro hole drilling in a silicon substrate using multi-bursts of nanosecond UV laser pulses, J. Micromech. Microeng. 16 (2006) 109–112.
[39] H. Matsumoto, Z. Lin, J. Kleinert, Ultrafast laser ablation of copper with ~GHz bursts, Proc. SPIE 10519 (2018), 1051902.
[40] D.J. Förster, S. Faas, S. Gröninger, F. Bauer, A. Michalowski, R. Weber, T. Graf, Shielding effects and re-deposition of material during processing of metals with bursts of ultra-short laser pulses, Appl. Surf. Sci. 440 (2018) 926–931.
[41] A. Bogaerts, Z. Chen, D. Autrique, Double pulse laser ablation and laser induced breakdown spectroscopy: a modeling investigation, Spectrochim. Acta Part B 63 (2008) 746–754.
[42] Q. Min, M.G. Su, B. Wang, L. Wu, S.Q. He, D.X. Sun, S.Q. Cao, C.Z. Dong, Investigation of the expansion dynamics of silicon plasmas generated by double nanosecond laser pulses, Phys. Plasma. 25 (2018), 073302.
[43] G.A. Bird, Molecular Gas Dynamics and the Direct Simulation of Gas Flows, Oxford University Press, New York, 1994.
[44] W. Wagner, A convergence proof for Bird's direct simulation Monte Carlo method for the Boltzmann equation, J. Stat. Phys. 66 (1992) 1011–1044.
[45] C. Cercignani, Rarefied Gas Dynamics: From Basic Concepts to Actual Calculations, Cambridge University Press, Cambridge, 2000.
[46] A.A. Ionin, S.I. Kudryashov, L.V. Seleznev, Near-critical phase explosion promoting breakdown plasma ignition during laser ablation of graphite, Phys. Rev. E 82 (2010), 016404.
[47] F. Sharipov, J.L. Strapasson, Direct simulation Monte Carlo method for an arbitrary intermolecular potential, Phys. Fluid. 24 (2012), 011703.
[48] V.A. Petrov, O.A. Ranjbar, P.A. Zhilyaev, A.N. Volkov, Kinetic simulations of laser-induced plume expansion from a copper target into a vacuum or argon background gas based on *ab initio* calculation of Cu-Cu, Ar-Ar, and Ar-Cu interactions, Phys. Fluid. 32 (2020), 102010.
[49] K.W. Kayang, A.N. Volkov, P.A. Zhilyaev, F. Sharipov, The *ab initio* potential energy curves of atom pairs and transport properties of high-temperature vapors of Cu and Si and their mixtures with He, Ar, and Xe gases, Phys. Chem. Chem. Phys. 25 (2023) 4872–4898.
[50] C. Cercignani, Theory and Application of the Boltzmann Equation, Scottish Academic Press, Edinburgh and London, 1975.
[51] S. Chandra, G.D. Scott, Condensation coefficients of silver, gold, and copper in vacuum deposition, Can. J. Phys. 36 (1958) 1148–1153.
[52] L. Bachmann, J.J. Shin, Measurement of the sticking coefficients of silver and gold in an ultrahigh vacuum, J. Appl. Phys. 37 (1966) 242–246.
[53] M.-C. Wu, W.S. Oh, D.W. Goodman, Initial sticking probabilities of Cu vacuum deposited on ordered Al_2O_3 and MgO, Surf. Sci. 330 (1995) 61–66.
[54] M. Aghaei, S. Mehrabian, S.H. Tavassoli, Simulation of nanosecond pulsed laser ablation of copper samples: a focus on laser induced plasma radiation, J. Appl. Phys. 104 (2008), 053303.
[55] R. Kelly, A. Miotello, Comments on explosive mechanisms of laser sputtering, Appl. Surf. Sci. 96-98 (1996) 205–215.
[56] D. Sibold, H.M. Urbassek, Monte Carlo study of Knudsen layers in evaporation from elemental and binary media, Phys. Fluids A: Fluid Dynam. 5 (1993) 243–256.
[57] C. Porneala, D.A. Willis, Observation of nanosecond laser-induced phase explosion in aluminum, Appl. Phys. Lett. 89 (2006), 211121.
[58] W.D. Bennon, F.P. Incopera, A continuum model for momentum, heat, and species transport in binary solid-liquid phase change systems – I. Model formulation, Int. J. Heat Mass Transfer 30 (1987) 2161–2170.
[59] N.M. Bulgakova, R. Stoian, A. Rosenfeld, I.V. Hertel, W. Marine, E.E.B. Campbell, A general continuum approach to describe fast electronic transport in pulsed laser irradiated materials: the problem of Coulomb explosion, Appl. Phys. A 81 (2005) 345–356.

[60] R.J. Le Roy, Y. Huang, C. Jary, An accurate analytic potential function for ground-state N_2 from a direct-potential-fit analysis of spectroscopic data, J. Chem. Phys. 125 (2006), 164310.
[61] L.I. Sedov, Similarity and Dimensional Methods in Mechanics, CRC Press, Boca Raton, 1993.
[62] See supplementary material to Ref. [26].
[63] A.K. Sharma, R.K. Thareja, Plume dynamics of laser-produced aluminum plasma in ambient nitrogen, Appl. Surf. Sci. 243 (2005) 68–75.
[64] S. Lafane, T. Kerdja, S. Abdelli-Messaci, S. Malek, M. Maaza, Laser-induced plasma study by fast imaging for $Sm_{1-x}Nd_xNiO_3$ thin film deposition, Appl. Phys. A. 98 (2010) 375–383.
[65] J. Wu, W. Wei, X. Li, S. Jia, A. Qiu, Infrared nanosecond laser-metal ablation in atmosphere: initial plasma during laser pulse and further expansion, Appl. Phys. Lett. 102 (2013), 164104.
[66] N. Farid, S.S. Harilal, H. Ding, A. Hassanein, Emission features and expansion dynamics of nanosecond laser ablation plumes at different ambient pressures, J. Appl. Phys. 115 (2014), 033107.
[67] W. Bauer, G.P. Perram, T. Haugan, Comparison of plume dynamics for laser ablated metals: al and Ti, J. Appl. Phys. 123 (2018), 095304.
[68] J. Thomas, H.C. Joshi, A. Kumar, R. Philip, Pulse width dependent dynamics of laser-induced plasma from a Ni thin film, J. Phys. D: Appl. Phys. 52 (2019), 135201.